



## Paleomagnetic analysis using SQUID microscopy

Benjamin P. Weiss,<sup>1</sup> Eduardo A. Lima,<sup>1,2</sup> Luis E. Fong,<sup>2</sup> and Franz J. Baudenbacher<sup>2,3</sup>

Received 16 January 2007; revised 14 May 2007; accepted 19 June 2007; published 19 September 2007.

[1] Superconducting quantum interference device (SQUID) microscopes are a new generation of instruments that map magnetic fields with unprecedented spatial resolution and moment sensitivity. Unlike standard rock magnetometers, SQUID microscopes map magnetic fields rather than measuring magnetic moments such that the sample magnetization pattern must be retrieved from source model fits to the measured field data. Here we present the first direct comparison between paleomagnetic analyses on natural samples using joint measurements from SQUID microscopy and moment magnetometry. We demonstrate that in combination with *a priori* geologic and petrographic data, SQUID microscopy can accurately characterize the magnetization of lunar glass spherules and Hawaiian basalt. The bulk moment magnitude and direction of these samples inferred from inversions of SQUID microscopy data match direct measurements on the same samples using moment magnetometry. In addition, these inversions provide unique constraints on the magnetization distribution within the sample. These measurements are among the most sensitive and highest resolution quantitative paleomagnetic studies of natural remanent magnetization to date. We expect that this technique will be able to extend many other standard paleomagnetic techniques to previously inaccessible microscale samples.

**Citation:** Weiss, B. P., E. A. Lima, L. E. Fong, and F. J. Baudenbacher (2007), Paleomagnetic analysis using SQUID microscopy, *J. Geophys. Res.*, 112, B09105, doi:10.1029/2007JB004940.

### 1. Introduction

[2] Superconducting quantum interference devices (SQUIDs) are the most sensitive magnetometers available for making quantitative measurements of magnetic fields [Braginski and Clarke, 2004; Wikswo, 2004]. Over the last two decades, SQUID moment magnetometers, which typically measure the three components of the moment of a  $\sim 1 \text{ cm}^3$  sample with a sensitivity of  $10^{-12} \text{ Am}^2$  [Clem *et al.*, 2006; Fagaly, 2006], have become standard in state-of-the-art paleomagnetism laboratories. These magnetometers measure only the net moment of the sample and cannot discern the potentially highly variable spatial distribution of microscale magnetization within the sample. Of late, a new generation of scanning superconducting magnetometers called SQUID microscopes has appeared that, instead of directly measuring a sample's net moment, generate high resolution, high sensitivity maps of the magnetic field above the sample. SQUID microscopes typically raster a micro-fabricated sensor at a constant height above a sample, measuring the vertical component of the magnetic field in a planar grid of locations.

[3] SQUID microscopes capable of measuring samples at cryogenic temperatures at very high spatial resolution ( $4 \mu\text{m}$  or better) have been in use for some time [Kirtley and Wikswo, 1999]. Such instruments have limited use for paleomagnetism since the samples must be cooled down below 80 K, which usually severely alters their natural remanent magnetization (NRM). At such low temperatures, many crystals that are superparamagnetic at room temperature become single domain (and possibly magnetized), and many common minerals experience phase changes or magnetic transitions (like hematite's Morin transition at  $\sim 260 \text{ K}$  and magnetite's Verwey transition at  $\sim 125 \text{ K}$ ). Until recently, SQUID microscopes capable of measuring room temperature samples were limited to spatial resolutions of several mm [Cochran *et al.*, 1993; Egli and Heller, 2000; Nowaczyk *et al.*, 1998; Thomas *et al.*, 1992].

[4] A decade ago, a new generation of SQUID microscopes capable of submillimeter resolution appeared, first using high-transition temperature (high- $T_c$ ) SQUIDs [Lee *et al.*, 1996; Wellstood *et al.*, 1997], and then using the more sensitive low-transition-temperature (low- $T_c$ ) SQUIDs [Baudenbacher *et al.*, 1998; Dechert *et al.*, 1999]. Among the first of these low- $T_c$  microscopes was that of Baudenbacher *et al.* [Baudenbacher *et al.*, 2002a, 2002b, 2003; Fong *et al.*, 2004, 2005] (hereafter, SQUID Microscope, or SM). The SM can now measure the field of room temperature samples with a spatial resolution of better than  $100 \mu\text{m}$  and  $S_B^{1/2} = 1.5 \text{ pT/Hz}^{1/2}$  at frequencies above  $\sim 0.5 \text{ Hz}$ , where  $S_B^{1/2}$  is the square root of the magnetic field spectral power density (which measures the magnitude of

<sup>1</sup>Department of Earth, Atmospheric, and Planetary Sciences, Massachusetts Institute of Technology, Cambridge, Massachusetts, USA.

<sup>2</sup>Department of Physics and Astronomy, Vanderbilt University, Nashville, Tennessee, USA.

<sup>3</sup>Department of Biomedical Engineering, Vanderbilt University, Nashville, Tennessee, USA.

the magnetic field noise fluctuations per root frequency interval). We quickly found the SQUID Microscope to be a powerful tool for paleomagnetic and geologic investigations [Weiss *et al.*, 2000, 2001, 2002; Gattacceca *et al.*, 2006].

[5] The SQUID Microscope can detect the fields of dipoles with moments weaker than  $10^{-15}$  Am<sup>2</sup>, making it more than three orders of magnitude more sensitive than the best superconducting moment magnetometers (see Appendix A). This impressive moment sensitivity means that SQUID microscopy offers two particular advantages with respect to moment magnetometry. First, SQUID microscopy can detect small, isolated samples and small magnetized regions within larger samples (rock fragments, dust particles, and single crystals) which, by virtue of their size, have weak magnetic moments. Second, SQUID microscopy can potentially be used to place constraints on the fine spatial variability of magnetization within a large-scale sample. These two advantages are linked in that SQUID microscopy is able to detect the fields of weak dipolar point sources as a result of its ability to map magnetic fields at high resolution [Weiss *et al.*, 2001]. Because the sensitivity of SQUID sensors to uniform fields scales with the size of the sensor area, this also means that SM is *less* sensitive than moment magnetometry to large (cm-sized) samples with spatially uniform magnetization.

[6] This possibility of mapping magnetization with high spatial resolution cannot be taken for granted: it is well known that magnetic field maps are not sufficient for uniquely inferring the spatial distribution of magnetization within the sample. The non-uniqueness of the magnetic inverse problem is intrinsic to Maxwell's equations rather than to SQUID microscopy techniques. This imposes limitations on the reconstruction algorithms that are inherent to magnetic data.

[7] For current distribution reconstructions, [Kress *et al.*, 2002] demonstrate that the null-space associated with the Biot-Savart operator is nontrivial. A nontrivial null-space means that multiple current distributions yield the same magnetic field, or equivalently, that there are current distributions which are magnetically silent. Those silent sources can be added to or subtracted from the original source without changing the overall magnetic field [Lima *et al.*, 2006]. Similarly, it is straightforward to verify the existence of different magnetization distributions which generate the same magnetic field. For instance, it is well known that the field outside of a uniformly magnetized sphere is identical to that of a magnetic dipole located at the center of the sphere. Consider two nested, centered spheres of different sizes that are each uniformly magnetized. Because their external magnetic fields each have the same dipolar geometry, it is clearly impossible to distinguish between the two sources based on magnetic field measurements made outside of the larger sphere. Furthermore, it is also impossible to distinguish those sources from their equivalent dipole.

[8] There are two main approaches to dealing with this nonuniqueness. A single magnetization solution can sometimes be obtained if additional geophysical or geochemical constraints are applied to the solution beyond simply requiring that the residual sum of squares is minimized [Aster *et al.*, 2005; Blakely, 1996; Hansen, 1998, 2001; Lima *et al.*, 2006; Parker, 1994]. A second approach is to solve for unique model properties that are shared by all

possible magnetization solutions [Parker, 1977]. For instance, field measurements over all space with infinitesimal spatial resolution and zero noise uniquely constrain the net moment of the sample [Parker, 1971, 1988; Parker *et al.*, 1987].

[9] A large variety of methods in both the space and frequency domains have been developed by the planetary remote sensing community to retrieve crustal magnetization from crustal field measurements [Langel and Hinze, 1998; Parker, 1994]. Frequency domain inversion techniques have recently been extended to inversions of SQUID microscopy imaging of current and magnetization distributions [Chatrathorn *et al.*, 2002; Egli and Heller, 2000; Fleet *et al.*, 2001; Roth *et al.*, 1989; Sepulveda *et al.*, 1994; Tan *et al.*, 1996; Wikswo, 1996]. However, all previous SQUID microscopy inversion techniques have focused on retrieving the special case of magnetization with only two components (e.g., current loops confined to the sample plane or, equivalently, magnetization solutions oriented perpendicular to the plane) rather than the magnetization distributions with components in all three spatial directions. In the two-dimensional case, a unique solution can be obtained from noise-free data because a continuity equation provides a second independent constraint linking the two unknown current or moment distribution components [Lima *et al.*, 2006], whereas no additional independent equation exists for the three dimensional case. To our knowledge, no SQUID microscopy spatial domain inversion techniques have been previously described.

[10] Here we present the first application of regularized space domain inversions to the SQUID microscopy problem of inverting magnetic field data for a full three dimensional magnetization distribution. We apply these techniques to two relatively simple kinds of geological samples: two  $\sim 100$   $\mu\text{m}$  diameter glass spherules from the Moon and a 30- $\mu\text{m}$  thin section of basalt from the Mauna Loa volcano. We show that using reasonable assumptions about the magnetization (as inferred from petrographic, rock magnetic and other geologic data), the net moment direction and intensity measured directly with a 2G Enterprises Superconducting Rock Magnetometer (2G) can be retrieved from a constrained least squares inversion of SQUID microscope field maps of these samples. The sensitivity and imaging capabilities of SQUID microscopy make it a powerful new paleomagnetic tool that is complementary to the net moment measurements provided by SQUID moment magnetometry.

## 2. Measurement Methods

[11] In a typical SM paleomagnetic application, we scan planar samples using a horizontal grid spacing of 50–100  $\mu\text{m}$  at a sample-to-sensor distance of 80–200  $\mu\text{m}$ . SM measurements of non-planar samples (like the lunar spherules described here) are sometimes taken at higher distances depending on the shape and roughness of the samples. To keep the scanning distance small and constant, we use a spring-loaded mechanism to push planar samples up against the sapphire window that separates the room temperature sample from the 4.2 K SQUID sensor [see Fong *et al.*, 2005, Figure 6]. We usually place a 2.5- $\mu\text{m}$  mylar film on top of the sample to reduce friction and avoid scratching its

surface. In this configuration, the SQUID Microscope is sufficiently sensitive that it can readily detect the magnetic fields of typical 30- $\mu\text{m}$  thin sections of rock.

[12] Thin sections are ideal for SQUID microscopy in that they (a) can later be analyzed with a wide variety of standard analytical tools that are valuable for constraining the nature of the magnetic carriers and petrography, (b) are sufficiently thin relative to the sensor-to-sample distance that their magnetization as imaged by the SM can be treated to a first approximation as being confined to an infinitely thin plane, thereby regularizing the inverse problem (see below), and (c) are sufficiently smooth that they can be scanned at a well-defined and constant sample-to-sensor distance without risking damage to the SM sapphire window. As such, we usually scan doubly polished thin sections specially prepared using a process designed to preserve the NRM. We use room temperature cyanoacrylate cement instead of heat-treated epoxy as a binder, all of our cutting and grinding is conducted using nonmagnetic blades and tools, we use amorphous silica as a final polishing step to remove any magnetostrictive surface layer [e.g., *Krasa*, 2002], and our sections are mounted on nonmagnetic GE 124 quartz slides. Our SM study of the basalt described below confirms that the thin section making process indeed did not substantially alter its NRM. Although it is possible that the thin section shape could impart some gross magnetic anisotropy to the sample, we did not observe this effect in the one anisotropy study we have conducted so far (on Martian meteorite ALH84001 [*Weiss et al.*, 2005]).

### 3. Least Squares Methods

[13] In the following section we develop the least squares equations for retrieving magnetization from SQUID microscopy data. Because both SQUID microscopy data and samples typically have a planar geometry, the equations are expressed in Cartesian coordinates. We begin in section 3.1 by presenting the general inverse problem of retrieving a three-component magnetization pattern from single-component magnetic field measurements of planar samples. In section 3.2 we discuss the restricted problem of fitting for an unresolved dipolar source of unknown location using nonlinear least squares techniques. Then in section 3.3 we review the matrix methods for solving the discretized linear least squares problem using the equivalent source formalism in which we make no assumptions about the magnetization solution beyond requiring that the dipole locations be fixed. We rely on the fact that an arbitrarily complex magnetization pattern can always be expressed as the sum one or more dipolar sources. As discussed in section 3.4, this problem is typically so ill-posed that without further constraints on the sample magnetization it is not practically useful. In sections 3.5 and 3.6 we reformulate the basic equations under the additional assumption of either a unidirectional magnetization or uniform magnetization.

#### 3.1. Magnetic Field of a Resolved Source: The Equivalent Source Formalism

[14] Nearly all existing SQUID microscopes (with the exception of [*Ketchen et al.*, 1997]) measure only the vertical component  $B_z$  of the magnetic field. Therefore we will restrict the discussion to inversion of  $B_z$  data only. At a

measurement position  $\vec{a} = (x_a, y_a, z_a)$  near a magnetized sample of volume  $V$  we have

$$B_z(\vec{a}) = \int_V \vec{G}_z(\vec{a}, \vec{b}) \cdot \vec{M}(\vec{b}) dV \quad (1)$$

where  $\vec{M}(\vec{b})$  is the magnetization at location  $\vec{b} = (x_b, y_b, z_b)$  within the sample and  $\vec{G}_z(\vec{a}, \vec{b})$  is the Green's function which expresses the dependence of the  $z$ -component of the magnetic field at the location  $\vec{a}$  on the magnetization element at location  $\vec{b}$ :

$$\vec{G}_z(\vec{a}, \vec{b}) = \frac{\mu_0}{4\pi} \frac{3\vec{r}(z_a - z_b) - r^2\hat{k}}{r^5} \quad (2)$$

Here  $\vec{r} = \vec{a} - \vec{b}$ ,  $\hat{k}$  is a unit vector oriented along the  $z$  axis (vertical), and  $\mu_0$  is the permeability of free space. Suppose the sample has no thickness in the vertical direction and is leveled (e.g., it is a point source or plane whose normal points toward the sensor). Setting  $x = x_a - x_b$ ,  $y = y_a - y_b$ , and  $z = z_a - z_b$  (= the constant sample-to-sensor distance,  $h$ ), we see that

$$B_z(\vec{a}) = \frac{\mu_0}{4\pi} \int_A \left[ \frac{3zx}{r^5} M'_x(x_b, y_b, z_b) + \frac{3zy}{r^5} M'_y(x_b, y_b, z_b) + \left( \frac{3z^2}{r^5} - \frac{1}{r^3} \right) M'_z(x_b, y_b, z_b) \right] dA \quad (3)$$

where  $A$  is the surface area of the sample, and  $M'_x$ ,  $M'_y$ , and  $M'_z$  are the three Cartesian components of the moment per unit area of the sample. Our approach is to discretize this integral by representing the magnetization as being due to  $Q$  individual dipole moments  $\vec{m}_j$  with field measurements  $B_{zi}$  at each of  $P$  locations:

$$B_{zi} = \sum_{j=1}^Q \vec{G}_{zij}(\vec{a}_i, \vec{b}_j) \cdot \vec{m}_j(\vec{b}_j) = \frac{\mu_0}{4\pi} \sum_{j=1}^Q \frac{3z_{ij}x_{ij}}{r_{ij}^5} m_{xj} + \frac{3z_{ij}y_{ij}}{r_{ij}^5} m_{yj} + \left( \frac{3z_{ij}^2}{r_{ij}^5} - \frac{1}{r_{ij}^3} \right) m_{zj} \quad (4)$$

where  $x_{ij} = x_{ai} - x_{bj}$ ,  $y_{ij} = y_{ai} - y_{bj}$ ,  $z_{ij} = z_{ai} - z_{bj}$  (=  $h$  for a planar sample),  $r_{ij} = \sqrt{x_{ij}^2 + y_{ij}^2 + z_{ij}^2}$ , and  $m_{xj}$ ,  $m_{yj}$ , and  $m_{zj}$  are the three Cartesian components of  $\vec{m}_j$ . Using  $m_{xj} = m_j \sin \theta_j \cos \phi_j$ ,  $m_{yj} = m_j \sin \theta_j \sin \phi_j$ , and  $m_{zj} = m_j \cos \theta_j$  where  $\theta$  and  $\phi$  are the direction angles of  $\vec{m}$ , we can also express (4) as

$$B_{zi}(\vec{a}) = \frac{\mu_0}{4\pi} \sum_{j=1}^Q \frac{3z_{ij}x_{ij}}{r_{ij}^5} m_j \sin \theta_j \cos \phi_j + \frac{3z_{ij}y_{ij}}{r_{ij}^5} m_j \sin \theta_j \sin \phi_j + \left( \frac{3z_{ij}^2}{r_{ij}^5} - \frac{1}{r_{ij}^3} \right) m_j \cos \theta_j \quad (5)$$

In the least squares approach we seek the set of moments  $\vec{m}_j^*$  which minimize the squared Euclidean norm of the difference between the data and model:

$$D^2 = \sum_{i=1}^P \left[ \hat{B}_{zi} - \sum_{j=1}^Q \vec{G}_{zij}(\vec{a}_i, \vec{b}_j) \cdot \vec{m}_j^*(\vec{b}_j) \right]^2 \quad (6)$$

where  $\hat{B}_{zi}$  are the (possibly noisy) measurements of the vertical component of the field. For our least squares fits presented in section 4, we calculate the residual root mean square (RMS) =  $D/\sqrt{P}$  as a measure of the misfit.

[15] The components  $B_{zi}$  are linear in  $m_x$ ,  $m_y$ , and  $m_z$  but are nonlinear functions of the position  $\vec{r}$  and dipole angular orientation  $\theta$  and  $\phi$ . Therefore for fixed dipole locations we can use standard linear least squares techniques to obtain the best fit Cartesian dipole moment components for a given set of Cartesian magnetic field data. This approach is known as the equivalent source formalism [Dampney, 1969; Emilia, 1973; Mayhew, 1979; Nicolosi et al., 2006; von Frese et al., 1981], which has long been in use for modeling geomagnetic anomalies but has not yet, to our knowledge, been

$$\mathbf{A} = \begin{bmatrix} \partial B_{z1}/\partial m_{x1} & \partial B_{z1}/\partial m_{y1} & \partial B_{z1}/\partial m_{z1} & \partial B_{z1}/\partial m_{x2} & \partial B_{z1}/\partial m_{y2} & \partial B_{z1}/\partial m_{z2} & \cdots & \partial B_{z1}/\partial m_{zQ} \\ \partial B_{z2}/\partial m_{x1} & & & & & & & \\ \partial B_{z3}/\partial m_{x1} & & & & & & & \vdots \\ \vdots & & & & & & & \\ \partial B_{zP}/\partial m_{x1} & & & \cdots & & & & \partial B_{zP}/\partial m_{zQ} \end{bmatrix}$$

adapted for SQUID microscopy. This is the technique we will use in section 3.3 to obtain constraints on the magnetization of the basalt thin section.

### 3.2. Net Moment of an Unresolved Source

[16] If the dipole positions are allowed to vary, the least squares problem is nonlinear. Because computational techniques for solving nonlinear problems are generally much less well developed than for linear problems, this is usually to be avoided. However, for sources composed of a small number of individually unresolved dipolar sources, this can be an extremely fast and powerful way of obtaining the sample magnetization. It is also unique [Lima et al., 2006].

[17] In section 4.2, we use this approach to solve for the net moments of two small lunar spherules each represented by a single dipole source using equation (5). We used a dipolar source because our samples are approximately spherical, and as previously noted the external field of a uniformly magnetized sphere is identical to that of a central point dipole of the same moment. In actuality, the spherule shapes depart from a perfect sphere by no more than  $\sim 30\%$  of their diameters ( $\sim 70 \mu\text{m}$ ). This is  $\sim 7$  times smaller than the sensor-to-sample distance such that the observed field is nearly purely dipolar. Fitting for the dipole moment therefore should give an excellent estimate of the mean magnetic moment of the spherule [Parker, 1971; Parker et al., 1987]. Our least squares fits validate this approximation because the residuals are within the measurement uncertainties (see section 4.2).

### 3.3. Unrestricted Solution

[18] Assume we have measurements of only the  $z$ -component of the magnetic field at  $P$  locations. In the case of SQUID microscopy, these are usually in a regular rectangular grid at a fixed height above the sample. We wish to fit for the three components of each of  $Q$  dipoles with fixed positions distributed throughout the sample, for a total of  $3Q$  parameters.

[19] As described above, this is a linear least squares problem which requires solving the system of equation (4).

This system can be expressed in matrix form  $\mathbf{A}\mathbf{d} = \hat{\mathbf{b}}$ , where  $\mathbf{A}$  is the  $M \times N$  Jacobian (also known as the Green's matrix or source function matrix),  $\mathbf{d}$  is an  $N \times 1$  vector containing the parameters, and  $\hat{\mathbf{b}}$  is an  $M \times 1$  vector containing the field measurements:

$$\mathbf{d} = [m_{x1} \ m_{y1} \ m_{z1} \ m_{x2} \ m_{y2} \ m_{z2} \ \cdots \ m_{zQ}]^T$$

and

$$\hat{\mathbf{b}} = [\hat{B}_{z1} \ \hat{B}_{z2} \ \cdots \ \hat{B}_{zP}]^T$$

The Jacobian is given by:

where from (4)

$$\begin{aligned} \partial B_{zi}/\partial m_{xi} &= \mu_0 3z_{ij}x_{ij}/4\pi r_{ij}^5 \\ \partial B_{zi}/\partial m_{yi} &= \mu_0 3z_{ij}y_{ij}/4\pi r_{ij}^5 \\ \partial B_{zi}/\partial m_{zi} &= \mu_0 3z_{ij}^2/4\pi r_{ij}^5 - \mu_0/4\pi r_{ij}^3 \end{aligned} \quad (7)$$

Here we have  $M = P$  and  $N = 3Q$ . In the linear least squares approach, we search for the solution  $\mathbf{d}^*$  which minimizes the Euclidean norm of the difference between the data and model  $\|\mathbf{A}\mathbf{d}^* - \hat{\mathbf{b}}\|$ .

[20] Solving equation (4) for an otherwise unconstrained magnetization solution is in general a rank-deficient problem since the unknown moment distribution  $\vec{m}_j$  may be a continuous function and therefore should be represented by an infinite number of dipoles rather than the finite matrix  $\mathbf{d}$  [Parker, 1977]. Only for certain moment distributions with special properties (i.e., those with no components in the plane of the sample [Roth et al., 1989], or those with a single dipole point source (e.g., lunar spherules) will there be a unique solution [Lima et al., 2006]. In the equivalent source scheme,  $Q$  is in practice limited to a value such that the spacing between dipoles is less than the distance of the dipoles to the sensor,  $h$  [Bott and Hutton, 1970; Langel et al., 1984; Mayhew, 1982; Mayhew and Galliher, 1982]. Even so, this often still leaves the unconstrained inverse problem ill-posed without some other form of regularization.

### 3.4. Approach to Nonuniqueness

[21] In the next two sections, we discuss two possible assumptions that can be made about the solution that regularize the inversion. Our approach is similar in philosophy to that developed by Parker for understanding shipborne magnetic surveys of seamounts [Hildebrand and Parker, 1987; Parker, 1988, 1991, 1994; Parker et al., 1987]. We seek to learn something about the magnetic properties and NRM of a geological sample from a set of measurements of its external magnetic field. Although there are infinitely many possible magnetization patterns inside of the sample

that can yield the observed field data set, additional constraints may enable us to eventually place bounds on the true magnetization which are useful for paleomagnetism. For instance, we can assess hypotheses that the magnetization is (i) uniform in intensity and orientation, (ii) unidirectional, or (iii) neither uniform nor unidirectional. We can select from among these possibilities by comparing the residual errors of the least squares fits for each of these cases with the expected measurement error. For some samples, as Parker found during his seamount inversions, depending on the nature of the magnetization and its intensity relative to instrument noise, we may not be able to distinguish between these possibilities, while for others the choice may be clear.

[22] Any additional information about the sample beyond that of the magnetic field measurements will further constrain the nature of the magnetization solution (and so may be used to distinguish among possibilities *i–iii*). In this regard, SQUID microscopy has a number of advantages relative to shipborne and satellite surveys. Here, we know the physical bounds of the sample to relatively high accuracy, need only solve for a magnetization distribution over two spatial dimensions rather than three (when measuring thin sections and unresolved sources), and have the possibility of obtaining a wealth of high resolution mineralogical and petrological data on the very same sample we are scanning using a wide variety of other analytical instruments.

[23] Also, we have yet another powerful tool at our disposal: we can give the sample an artificial magnetization in a known direction in the laboratory. This gives us two additional advantages. First, it permits us to use SQUID microscopy to infer the rock magnetic properties of the sample, which indirectly constrains the mineralogy of the magnetic sources. Secondly, if we magnetize the sample in the vertical direction (for instance by giving it a saturation isothermal remanent magnetization (sIRM)), then in the case of perfect measurements we can then uniquely solve for the sIRM by requiring the moment to be vertical and simply fitting for intensity. This is analogous to solving for planar current distributions [Egli and Heller, 2000; Fleet et al., 2001; Lima et al., 2006; Roth et al., 1989]. If we can assume that the sources carrying the imposed magnetization were also carrying the NRM, then the knowledge of the locations of the sources in the artificial magnetization scan can also be used to constrain the locations of the sources in the NRM map. In this way, the number of dipoles used in the equivalent source scheme could be reduced, thereby regularizing the NRM solution and also saving computation time.

### 3.5. Unidirectional Solution

[24] Suppose we fix the orientation of all the dipoles in a single direction ( $\theta, \phi$ ) while letting their magnitudes independently vary. By fixing the moment orientation, it is then natural to require the individual moments to always be nonnegative ( $m_j \geq 0$  for all  $j$ ). This magnetization, which is unidirectional (uniform in direction) but nonuniform in intensity [Emilia and Massey, 1974; McNutt, 1986; Parker, 1991], has

$$\mathbf{d} = [m_1 \ m_2 \ \cdots \ m_Q]^T$$

and

$$\mathbf{A} = \begin{bmatrix} \partial B_{z1}/\partial m_1 & \partial B_{z1}/\partial m_2 & \cdots & \partial B_{z1}/\partial m_Q \\ \partial B_{z2}/\partial m_1 & & & \\ \vdots & & & \\ \partial B_{zP}/\partial m_1 & & \cdots & \partial B_{zP}/\partial m_Q \end{bmatrix}$$

where the entries in  $A$  are now given by:

$$\begin{aligned} \frac{\partial B_{zi}}{\partial m_j} &= \frac{\mu_0}{4\pi} \frac{3z_{ij}x_{ij}}{r_{ij}^5} \sin \theta \cos \phi + \frac{\mu_0}{4\pi} \frac{3z_{ij}y_{ij}}{r_{ij}^5} \sin \theta \sin \phi \\ &+ \frac{\mu_0}{4\pi} \left( \frac{3z_{ij}^2}{r_{ij}^5} - \frac{1}{r_{ij}^3} \right) \cos \theta \end{aligned} \quad (8)$$

We see that for all  $j$ ,

$$m_{zj} = \frac{\cot \theta}{\cos \phi} m_{yj} \text{ and } m_{yj} = m_{xj} \tan \phi \quad (9)$$

so that although we still have  $M = P$  measurements, we now have only  $N = Q$  parameters to fit because of the  $2Q$  additional constraints imposed by (9). Note that by requiring the moments to be unidirectional and nonnegative, there is no longer a guarantee that a solution exists whose residual RMS is less than our measurement uncertainty [Parker, 1991]. This permits us to test the hypothesis that the magnetization in a sample is unidirectional.

### 3.6. Uniform Solution

[25] Suppose we make the strict requirement that all the dipoles not only must have the same direction but also have identical moment intensities. Assuming the dipoles are uniformly distributed throughout the sample, this is the uniform magnetization solution first described by Vacquier [Vacquier, 1962]. Here we simply have

$$\mathbf{d} = [m_x \ m_y \ m_z]^T$$

and

$$\mathbf{A} = \begin{bmatrix} \partial B_{z1}/\partial m_x & \partial B_{z1}/\partial m_y & \partial B_{z1}/\partial m_z \\ \partial B_{z2}/\partial m_x & \partial B_{z2}/\partial m_y & \partial B_{z2}/\partial m_z \\ \vdots & \vdots & \vdots \\ \partial B_{zP}/\partial m_x & \partial B_{zP}/\partial m_y & \partial B_{zP}/\partial m_z \end{bmatrix}$$

where the entries in  $A$  are given by:

$$\begin{aligned} \partial B_{zi}/\partial m_x &= \frac{3\mu_0}{4\pi} \sum_{j=1}^Q z_{ij}x_{ij}/r_{ij}^5 \\ \partial B_{zi}/\partial m_y &= \frac{3\mu_0}{4\pi} \sum_{j=1}^Q z_{ij}y_{ij}/r_{ij}^5 \\ \partial B_{zi}/\partial m_z &= \frac{\mu_0}{4\pi} \sum_{j=1}^Q 3z_{ij}^2/r_{ij}^5 - 1/r_{ij}^3 \end{aligned} \quad (10)$$

We still have  $M = P$  measurements but now have only  $M = 3$  parameters to fit. Once again, there is no longer a guarantee that a solution exists whose residual RMS is less than our

measurement uncertainty [Parker, 1991]. This permits us to test the hypothesis that the magnetization in a sample is uniform.

#### 4. Application to Geological Samples

[26] We now describe paleomagnetic analyses of two kinds of geological samples that are representative of science targets ideally suited for SQUID microscopy: two lunar glass spherules (unresolved dipole sources with extremely weak magnetization) and a  $\sim 1.5$  cm diameter 30- $\mu\text{m}$  thin section of Hawaiian basalt (a resolved source with a spatially variable magnetization distribution). By implementing the techniques described in section 3, we placed constraints on the magnetization within these samples from SQUID Microscope field measurements in combination with contextual constraints from petrography, geochronology, and direct moment measurements using both a 2G Enterprises Superconducting Rock Magnetometer and a borehole fluxgate magnetometer (2G). A comparison between the SM, 2G and borehole magnetometry data demonstrates that in the case of the present two samples, SQUID microscopy can be used to recover paleomagnetic directions and magnitudes that match those measured directly by standard moment magnetometers.

##### 4.1. Measurement Methods

[27] Moment magnetometry measurements were taken with a 2G Enterprises Superconducting Rock Magnetometer 760 inside a magnetically shielded room with a single layer of transform steel (DC field  $<1000$  nT). Because its three pairs of sensory Helmholtz coils envelop the sample, the 2G uniquely measures the net magnitude and direction of sample moment. Although the weakest moment detectable with the 2G is  $10^{-12}$  Am<sup>2</sup>, the nonuniformity of the response of the 2G Helmholtz pickup coils means that even for stronger moments the accuracy is limited to  $\sim 1-5\%$  for cm<sup>3</sup>-sized samples [Kirschvink, 1992]. Because 2G measurements are fairly standard, we refer the reader to [Clem *et al.*, 2006; Fagaly, 2006; Fuller *et al.*, 1985] for further details.

[28] The SQUID Microscope was used to measure the vertical component of the magnetic field in a uniform rectangular grid pattern at a constant height above the samples [see Weiss *et al.*, 2001, 2002; Baudenbacher *et al.*, 2002a, 2003; Fong *et al.*, 2005; Gattaceca *et al.*, 2006]. The scans of both the spherules and basalt were conducted inside a three  $\mu$ -metal layer magnetically shielded room with DC field  $<50$  nT. The end of each scanning line was preset to be several mm beyond the sample edge such that the field from the sample at the endpoints is negligible. The voltage measured in this zero field region, as well as its first derivative (estimated from the difference between the zero field voltages measured at the beginning of adjacent scanning lines), were each subtracted from the data in each scanning line. All of the scans presented here and associated analyses are from data sets preprocessed in this way.

[29] All of the SM measurements presented here were also conducted at sample-to-sensor distances which exceeded the sensor diameter. In this configuration, the spatial resolution of the measurements is limited by the smoothing effect of scanning a harmonic field at a distance rather than by the horizontal averaging from the finite sensor diameter. As a result, we found in practice that there was little benefit to be gained from deconvolving the effect of the finite sensor diameter from the magnetic fields scans [Lima *et al.*, 2006; Roth *et al.*, 1989] (for a contrasting scenario, see [Egli and Heller, 2000]). This is not true for closer sample-to-sensor distances, and so we expect deconvolution will play an important role in our data analysis techniques in the future.

##### 4.2. Lunar Glass Spherules

[30] Our analyses of two lunar glass spherules demonstrate the power of SQUID microscopy to detect the moments of extremely weakly magnetic unresolved samples. The spherules, labeled 1 and 2, had diameters of 110 and 220  $\mu\text{m}$ , respectively, and were taken from regolith sample 14163 from at the Apollo 14 landing site [Cavarretta *et al.*, 1972; Labotka *et al.*, 1980]. This regolith forms part of the Fra Mauro Formation, is enriched in KREEP-type materials

**Figure 1.** SQUID Microscope (SM) measurements of two lunar glass spherules from Apollo 14 regolith sample 14163. Shown is the vertical component of the magnetic field as measured  $\sim 500$   $\mu\text{m}$  above the centers of the spherules. (a) Scan of the natural remanent magnetization (NRM) field of Spherule 1. The black circle shows the approximate shape and location of the spherule with respect to the scan. (b) Forward modeled SM scan using best fit parameters for the NRM of Spherule 1 (see Table 1). (c) Residuals for least squares NRM fit to Spherule 1 (difference between scans in (a) and (b)). (d) Scan of Spherule 1 after it had been exposed to a saturating magnetic field (600 mT) oriented toward the top of the page as shown. This is the saturation isothermal remanent magnetization (sIRM) field. The black circle shows the approximate shape and location of the spherule with respect to the scan. (e) Forward modeled SM scan using best fit parameters for the sIRM of Spherule 1 (see Table 1). (f) Residuals for least squares sIRM fit to Spherule 1 (difference between scans in (d) and (e)). (g) Scan of the NRM field of Spherule 2. The black circle shows the approximate shape and location of the spherule with respect to the scan. (h) Forward modeled SM scan using best fit parameters for the NRM of Spherule 2 (see Table 1). (i) Residuals for least squares NRM fit to Spherule 2 (difference between scans in (g) and (h)). (j) Scan of the sIRM field of Spherule 2. The black circle shows the approximate shape and location of the spherule with respect to the scan. (k) Forward modeled SM scan using best fit parameters for the sIRM of Spherule 2 (see Table 1). (l) Residuals for least squares sIRM fit to Spherule 2 (difference between scans in (j) and (k)). (m) Equal area plot showing average of four repeat 2G sIRM measurements on Spherule 1 and SM NRM and sIRM measurements for Spherule 1 (b,e) (black circles) and Spherule 2 (h, k) (grey circles). These directions are listed in Table 1. Filled circles are on the lower hemisphere and open circles are on the upper hemisphere. Scale bar for (a-l) is 0.5 mm. Note that the scans pictured here are actually extracted from the central portion of the full scans used for the inversion. The surrounding data points have near zero field values (no more than a few % of the peak values in the shown scans).

and is interpreted as being predominantly ejecta from the impact that formed the Imbrium basin. Compositional analyses of the spherules in this sample showed that they are mostly impact rather than volcanic melts and range in age from nearly 0 to 4 B.y. [Culler *et al.*, 2000; Levine *et al.*, 2005]. The spherules were sieved from the regolith, washed with alcohol to remove any surface contamination and then embedded with cyanoacrylate cement into a pure nonmagnetic quartz mount for magnetic measurements.

**4.2.1. SM Measurements**

[31] SM measurements of the spherules were acquired using a 250- $\mu\text{m}$  diameter superconducting pickup coil inductively coupled to a Quantum Design DC SQUID. We analyzed the lunar spherules primarily because we were interested in testing the capability of SQUID microscopy for

studying unresolved dipoles. However, the two spherules are much thicker than the basalt thin section and have diameters that differ significantly from one another. Therefore to insure that the spherules appeared as unresolved dipole sources to the SM, the sample-to-sensor distance for both spherules was set to a relatively large value ( $\sim 500 \mu\text{m}$ , more than twice the spherule diameters). SM measurements showed that NRM field of Spherule 1 at this distance was of several tens of nT, while that of Spherule 2 was 100 times weaker (Figures 1a and 1g).

[32] Following the methods described in section 3.2, we conducted nonlinear least squares fits to the SM data using the Levenberg-Marquardt method [Press *et al.*, 1992] to retrieve six parameters describing the net dipole moment of each spherule: the moment intensity, declination, inclina-

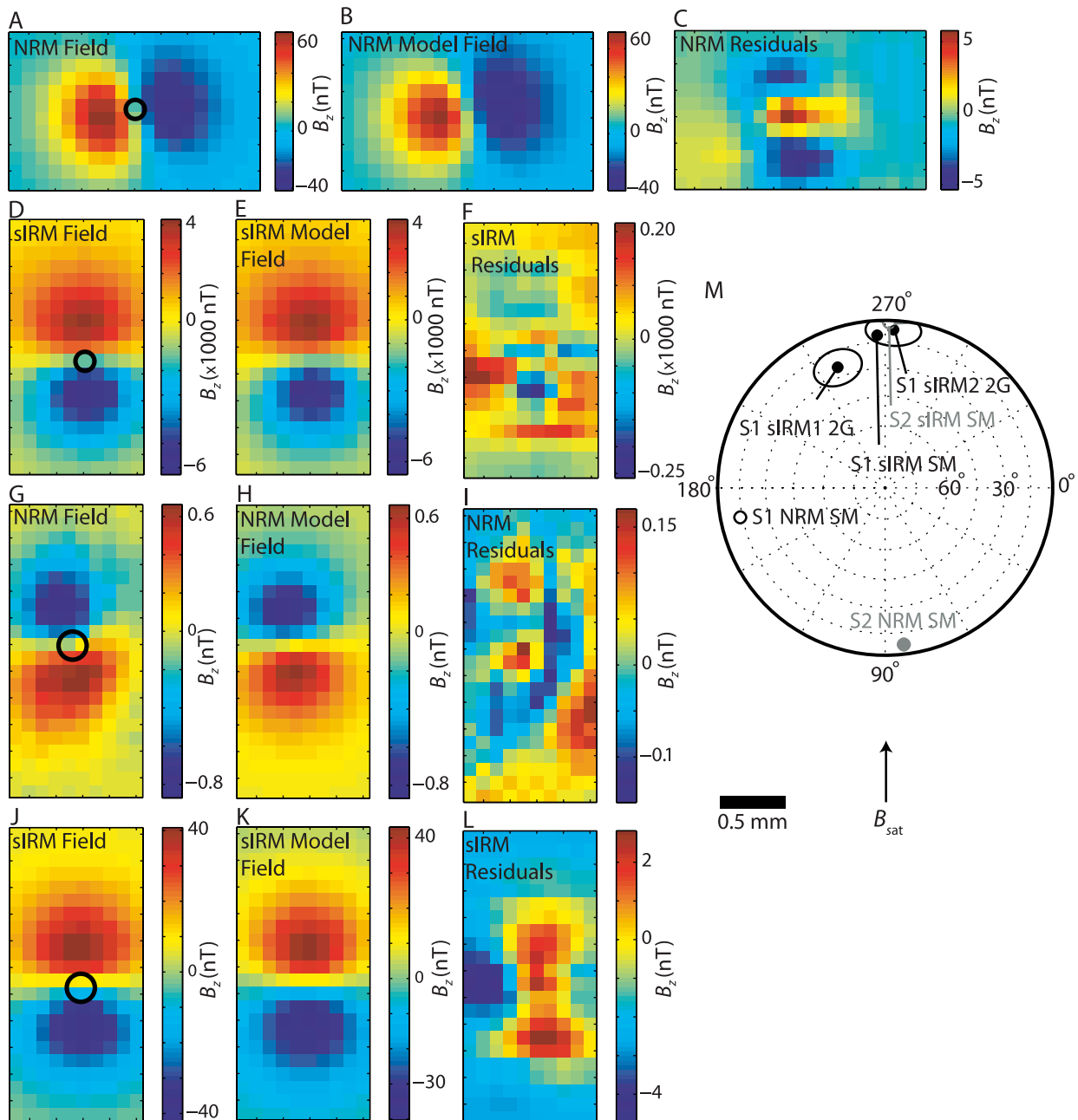


**Figure 1**

**Table 1.** Summary of Paleomagnetic Analyses of Two Lunar Spherules<sup>a</sup>

Sample	Remanence	Instrument	$M$	$N$	$Q$	$m$ , Am <sup>2</sup>	$i$ , °	$\delta$ , °	Residual RMS, nT
Spherule 1	NRM	SM	1170	6	1	$6.9 \times 10^{-11}$	-14	168	0.76
Spherule 2	NRM	SM	260	6	1	$8.6 \times 10^{-13}$	8	83	0.06
Spherule 1	sIRM	SM	810	6	1	$7.5 \times 10^{-9}$	11	267	48
Spherule 1	sIRM	2G	-	-	-	$1.3 \times 10^{-8}$	$7 \pm 9$	$273 \pm 9$	-
Spherule 2	sIRM	SM	494	6	1	$8.8 \times 10^{-11}$	-2	89	2.4

<sup>a</sup>The first column lists the name of the sample, followed in the next two columns by the type of remanence (natural remanent magnetization (NRM) or saturation isothermal remanent magnetization (sIRM)) and the instrument with which it was measured. The sIRM was produced by the application of a saturating field oriented toward  $i = 0$ ,  $\delta = 270^\circ$ . The next three columns specify the number of data points in the fit scan,  $M$ , the number of parameters,  $N$ , and the number of dipoles,  $Q$ . The last four columns give the moment as a result of the least squares fits (for SM scans) or direct measurements (for the 2G). Here  $m$  = dipole moment,  $i$  = inclination,  $\delta$  = clockwise declination (right =  $0^\circ$ ). The moment listed for the 2G are the average and circular standard deviation of four repeated measurements, each preceded by a reapplication of the saturating field.

tion, two horizontal position coordinates and vertical distance from the sensor. We fit for the three position coordinates of the dipole because the location of each spherule was imprecisely known and we found in practice that making this a free variable reduced our residual RMS without destabilizing the solution.

[33] The NRM fits are shown in Figures 1b, 1h and the fit parameters listed in Table 1. The moment of Spherule 2 is  $8.6 \times 10^{-13}$  Am<sup>2</sup>, which is below the sensitivity of the 2G. The noise level of the SM scan far away from the dipole is 0.05–1 nT (see the uncorrelated variations in pixel intensity at lower right corner of Figures 1g and 1i), about 10 times less than the field of the spherule. Given that this scan was measured at a sensor-to-sample distance 5 times greater than our minimum currently achievable distance, the cubic falloff of dipole fields with distance means that we can detect dipoles with moments  $10^3$  times weaker than that of Spherule 2. This exemplifies (although of course does not prove) the SM system noise level of  $10^{-15}$  Am<sup>2</sup> quoted in section 1.

[34] The NRM fit for Spherule 2 was the only spherule fit whose residual intensities were at the instrument noise level (Figure 1i) and normally distributed to >95% confidence according to the Jarque-Bera test [Judge *et al.*, 1988]. In contrast, the NRM residuals for Spherule 1 were about a factor of 8 above the sensor noise, have a non-Gaussian intensity distribution, and most importantly are spatially correlated. (Figure 1c).

[35] Following the NRM measurements, the spherules were given a saturation isothermal remanent magnetization by briefly exposing them to a 600 mT field in the scanning plane toward the top of the page. The spherules were then scanned with the SM again (Figures 1d and 1j). Least squares fitting (Figures 1e, 1f, 1k, and 1l) showed that the moments had increased by two orders of magnitude and rotated into alignment with the applied field (Table 1). The sIRM residuals for both spherules were again above the sensor noise, did not pass the Jarque-Bera test for being normally distributed at the 95% confidence level, and were highly spatially correlated.

[36] All but one of our spherule scans had spatially correlated residuals with intensities exceeding the SQUID sensor noise. One possible explanation for the high residuals is that they result from our idealized approximation of the spherules as magnetized spheres. However, a series of least squares experiments on artificial data (not shown) demonstrated that even if the spherule shapes were so

distorted as to have length-to-width ratios as great as 2:1, this still would lead to residuals with intensities only  $\sim 1\%$  of the data. As described in Appendix A, the computed residuals have roughly the intensity expected from position noise. Position noise, which scales with moment intensity, would also explain why the much weaker NRM of Spherule 2 does *not* have high intensity, spatially correlated residuals.

#### 4.2.2. 2G Measurements

[37] After storage in a magnetically shielded lab for six months, Spherule 1 was measured with the 2G. The intensity was found to be about half and the direction  $20^\circ$  divergent from that inferred from the SM scan of the sIRM (Figure 1m). Given the abundant superparamagnetic iron in lunar glasses [Fuller and Cisowski, 1987], these differences are almost certainly due to viscous decay of the spherule's moment. Therefore we again exposed the spherule to an intense magnetic field (370 mT) and remeasured it immediately with the 2G. The average of this and three more repeated applications of the field followed by 2G measurements gave a moment intensity and direction that matched that of the SM within the uncertainty associated with the superparamagnetic decay of the moment. This simple experiment is the first direct demonstration that moment measurements inferred from SQUID microscopy match measurements on the same sample with a standard moment magnetometer.

### 4.3. Basalt Thin Section

#### 4.3.1. Sample Description

[38] This 30- $\mu$ m thin section of tholeiitic basalt was taken from the Hawaii Scientific Drilling Project (HSDP) 2 core through the Mauna Kea volcano, Hawaii. The sample is from the interior of an aphyric pillow originating from a depth of 2421.4 m below sea level (core box 829, run 828) [DePaolo *et al.*, 1999]. Like the rest of the HSDP core, our sample is geographically oriented in inclination but not declination. Rock magnetic studies of samples from this part of the HSDP2 core indicate that the primary remanence carrier is pseudo single domain titanomagnetite ( $x\text{Fe}_2\text{TiO}_4 \cdot (1-x)\text{Fe}_3\text{O}_4$  with  $x \sim 0.6$ ) with a Curie temperature of 100–200°C, a bulk coercivity of  $\sim 20$  mT, and a squareness (ratio of saturation remanence to saturation magnetization) of  $\sim 0.4$  [Konny *et al.*, 2003; Tauxe and Love, 2003]. Thellier-Thellier paleointensity studies of pillow interior samples from this depth indicate that the remanence is almost entirely a viscous remanent magnetization (VRM) that formed in a field with a paleointensity of 50–60  $\mu$ T

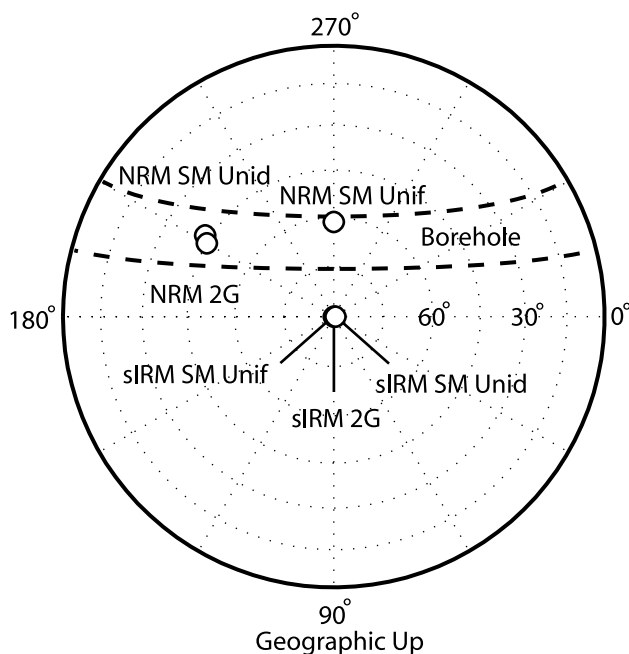


**Figure 2.** Equal area plot showing natural remanent magnetization (NRM) and saturation isothermal remanent magnetization (sIRM) directions of the basalt thin section obtained from least squares magnetization fits to SQUID Microscope (SM) scans and compared to direct measurements with a 2G Enterprises Superconducting Rock Magnetometer (2G) and Hawaii Scientific Drilling Project 2 borehole logging with a fluxgate magnetometer. The directions are plotted in thin section coordinates (for which geographic up is  $i = 0^\circ$  and  $\delta = 90^\circ$ ) and are listed in Table 2. Open (closed) symbols represent upper (lower hemisphere). The borehole inclination data (Steveling, personal communication) were measured from the same depth range as the basalt sample; transformed into thin section coordinates, these inclination data map as a minor circle band on the equal area plot (boundaries delineated by two dashed lines). The inclination for the SM fits to the sIRM field was forced to  $-90^\circ$ .

[Tauxe and Love, 2003]. By analogy with previous compositional studies of HSDP basalts [Baker et al., 1996], our sample consists of predominantly a groundmass of olivine, pyroxene, plagioclase, chromian spinel, and titanomagnetite and has abundant vesicles filled with a variety of essentially nonmagnetic secondary minerals (i.e., zeolites, smectite, apatite, and Ca-silicates [Walton and Schiffman, 2003]). The results of [Sharp and Renne, 2005] indicate that it has an  $^{40}\text{Ar}/^{39}\text{Ar}$  age of extrusion of  $\sim 500$  ka.

[39] Our basalt thin section has a surface area of several  $\text{cm}^2$  and was prepared using cyanoacrylate cement (without any heating) and mounted on a pure quartz slide (see section 2 for more details). Its NRM and sIRM were each measured with the SM. We found that the thin section was sufficiently magnetic that we were also able to measure both its NRM and sIRM with the 2G.

#### 4.3.2. 2G and Borehole Measurements

[40] We begin by summarizing the moment magnetometry measurements (Figure 2). In thin section coordinates, the 2G measured an NRM of  $m = 6.4 \times 10^{-8} \text{ Am}^2$ , inclination  $i = -45 \pm 3^\circ$  and clockwise declination  $\delta = 210 \pm 3^\circ$  and an sIRM of  $m = 2.2 \times 10^{-6} \text{ Am}^2$ , inclination  $i = -90 \pm 1^\circ$  and clockwise declination  $\delta = 2 \pm 1^\circ$  (angular uncertainties are one circular standard deviation) (Table 2, Figure 2). Transformed into geographic coordinates, the 2G NRM direction corresponds to an inclination of  $i' = 22.0 \pm 3^\circ$ , which is in excellent agreement with the HSDP2 borehole fluxgate inclination (averaged over the depths 2423.3–2423.5 m) of

$i' = 22.3^\circ$  [Steveling, 2006; Steveling et al., 2003] (Table 2, Figure 2).

#### 4.3.3. SM Measurements

[41] All SM measurements were taken at a scanning height of  $190 \mu\text{m}$  using a  $120 \mu\text{m}$  diameter monolithic DC SQUID sensor [Baudenbacher et al., 2003]. In this configuration, our effective spatial resolution is limited by the scanning height to about  $\sim 200 \mu\text{m}$ . Since the sample has a diameter of  $>1$  cm, this measurement configuration meant that the sample's magnetic field was spatially well-resolved and is highly nondipolar (Figures 3 and 4). Because the sIRM was created in the laboratory with a known field direction, we begin with the discussion of this scan and leave the more unconstrained NRM for later.

##### 4.3.3.1. sIRM

[42] The sIRM magnetic field (Figure 3) is complex, with highly variable intensity and numerous zero-crossings. The regions of upward and downward fields are correlated on a spatial scale of several mm, much larger than our estimated  $\sim 200 \mu\text{m}$  spatial resolution. A comparison of the scan (Figure 3b) with the optical photo of the sample (Figure 3a) clearly shows that the regions with  $B_z > 0$  correspond almost exclusively to the dark groundmass, whereas regions with  $B_z < 0$  correspond to the vesicles, the thin section edges, and the subhorizontal crack across the bottom third of the section. This field complexity far exceeds the magnetic anomalies observed by shipborne surveys for seamounts. This is an important difference, because this thin section is

**Table 2.** Summary of Paleomagnetic Analyses of Basalt Thin Section From Hawaii Scientific Drilling Project 2<sup>a</sup>

Remanence	Instrument	Fit Type	$M$	$N$	$Q$	$m$ , Am <sup>2</sup>	$i$	$i'$ (°)	$\delta$ (°)	Residual RMS (nT)
NRM	SM	Uniform	25,976	3	20,439	$6.5 \times 10^{-8}$	-61	29	270	$2.27 \times 10^4$
NRM	SM	Unidirectional	25,976	8749/ 25,976	8749/ 25,976	$2.6 \times 10^{-8}$ / $9.0 \times 10^{-8}$	-43	22	212	75/14
NRM	2G	-	-	-	-	$6.4 \times 10^{-8}$	$-45 \pm 3$	$22 \pm 3$	$210 \pm 3$	-
sIRM	SM	Uniform	25,976	3	20,439	$1.9 \times 10^{-6}$	-90	0	1	$7.2 \times 10^5$
sIRM	SM	Unidirectional	25,976	25,976	25,976	$1.6 \times 10^{-6}$	-90	0	0	1140
sIRM	2G	-	-	-	-	$2.2 \times 10^{-6}$	$-90 \pm 1$	$0 \pm 1$	$2 \pm 1$	-

<sup>a</sup>The first two columns list the type of remanence (natural remanent magnetization (NRM) or saturation isothermal remanent magnetization (sIRM)) and the instrument with which it was measured. The sIRM was produced by the application of a saturating field oriented toward  $i = -90^\circ$ . Because the resulting sIRM direction is known, the inclination for the sIRM fits was forced to  $-90^\circ$ . The third column lists the form of the magnetization solution assumed for least squares fits to the SM scans. The next three columns specify the number of data points in the fit scan  $M$ , the number of parameters  $N$ , and the number of dipoles  $Q$ . The last five columns give the moment as a result of the least squares fits (for SM scans) or direct measurements (for the 2G). Here  $m$  = dipole moment,  $i$  = inclination in thin section coordinates,  $i'$  = inclination in geographic coordinates,  $\delta$  = clockwise declination (right =  $0^\circ$ ). The angular uncertainties for the 2G moment orientations are one circular standard deviation.

taken from the subaqueous portion of the HSDP2 core and so was part of Mauna Kea when that volcano was just such a seamount! Of course, the reason for the higher field complexity of the SM scan relative to the ship surveys is the factor of  $10^7$  difference in sample-to-sensor distance.

[43] Decades of least squares analyses of magnetic survey data and paleomagnetic analyses of seamount rocks have shown that a uniform magnetization model provides a poor description for seamounts, even for those formed during a single polarity chron [Gee *et al.*, 1989; Kono, 1977; Parker *et al.*, 1987]. We therefore hardly expected it to be a good model for the SM scan. As shown below, this was clearly borne out by our magnetization inversions.

[44] Using an equivalent source approach (section 3) and assuming a uniform magnetization solution, we fit for the three components of each of  $Q = 20,439$  dipoles distributed in a grid whose boundaries coincide with the edges of the thin section. These edges were determined from a visual inspection of an optical photo of the section spatially registered with respect to the SM scan. The dipole grid spacing was set to  $100 \mu\text{m}$  (about half the sensor-to-sample distance such that the magnetization can be captured at high spatial resolution but without the instabilities that set in for finer spacings) and the horizontal position of each dipole was located directly under each measurement. All least

squares fits to the basalt were computed in MATLAB using the large-scale algorithms that are part of the *lsqclin* function (we found that the nonnegative least squares routine *lsqnonneg*, used by Parker [Parker, 1991] for his unidirectional solution, to be far too slow for use with our relatively much larger data sets). The heart of *lsqclin* is a preconditioned conjugate gradient analysis subroutine [Press *et al.*, 1992; Purucker *et al.*, 1996] that is computationally efficient when used with sparse matrices.

[45] Because the uniform solution requires fitting for only  $N = 3$  parameters ( $m_x$ ,  $m_y$  and  $m_z$ ), by far the most computationally intensive part of the process is calculating the Jacobian  $\mathbf{A}$  (equation (10)). This time can be reduced by computing an approximation of the Jacobian,  $\mathbf{A}^\dagger$ , by truncating the long-range interactions of the dipole moments: all elements  $A_{ij}$  for which dipole-datum distances  $r_{ij}$  exceeded some threshold,  $r_0$ , were set to zero. This truncation, commonly used for inverting large satellite magnetic field data sets [Purucker *et al.*, 1996], is even more useful for our unidirectional solutions described below; truncation permits the unidirectional Jacobians to be not only calculated more quickly but much more importantly makes them sparse. This sparsity dramatically reduced our memory requirements and permitted us to take advantage of fast matrix arithmetic techniques. We empirically determined the opti-

**Figure 3.** SQUID Microscope measurements and analysis of of the saturation isothermal remanent magnetization (sIRM) of a  $30\text{-}\mu\text{m}$  thin section of basalt from the Hawaii Scientific Drilling Project 2 deep drill core taken through the Mauna Kea volcano, Hawaii. (a) Reflected light photograph of thin section, showing groundmass of olivine, clinopyroxene, plagioclase, and titanomagnetite (dark areas) and numerous clear vesicles containing relatively nonmagnetic secondary minerals, primarily zeolites. (b) Scan showing the vertical component of the magnetic field  $\sim 190 \mu\text{m}$  above the sample. (c) Top: Computed vertical component of the magnetic field  $190 \mu\text{m}$  above a dipole with same moment and orientation as the net sIRM of the thin section (Table 2). Colorbar ranges from  $-150$  to  $200 \times 10^5$  nT. Bottom: Computed vertical component of the magnetic field  $190 \mu\text{m}$  above a  $2 \text{ mm} \times 2 \text{ mm}$  plate with same total moment and orientation as the net sIRM of the thin section. Colorbar ranges from  $-6$  to  $6 \times 10^5$  nT. (d) Estimated forward model,  $\mathbf{A}^\dagger \mathbf{d}$ , of the sIRM field (b) using the best fit unidirectional magnetization solution (for which the moments were forced to have inclination  $-90^\circ$ ) with  $r_0 = 6 \text{ mm}$ . (e) Estimated residuals,  $\mathbf{A}^\dagger \mathbf{d}^* - \mathbf{b}$ , for the best fit sIRM unidirectional moment solution (difference between matrices imaged in (b) and (d)). (f) Best fit moments,  $\mathbf{d}^*$ , of each of 25,976 dipoles associated with the unidirectional magnetization model field in (d). This map also depicts the magnetization when normalized to sample volume ( $3 \times 10^{-13} \text{ m}^3$  per dipole). (g) Estimated forward model,  $\mathbf{A}^\dagger \mathbf{d}$ , of the sIRM field (b) using the best fit uniform magnetization solution with  $r_0 = 6 \text{ mm}$ . The magnetization direction was unconstrained for this solution. (h) Estimated residuals,  $\mathbf{A}^\dagger \mathbf{d}^* - \mathbf{b}$ , for the best fit sIRM uniform moment solution (difference between matrices imaged in (b) and (g)). (i) Best fit moments,  $\mathbf{d}^*$ , of each of 20,439 dipoles (and magnetization) associated with the uniform magnetization model field in (g). Scale bars in (b, d–i) are  $2 \text{ mm}$  and in (c) are  $0.5 \text{ mm}$ . Geographic up is toward the bottom of the page.

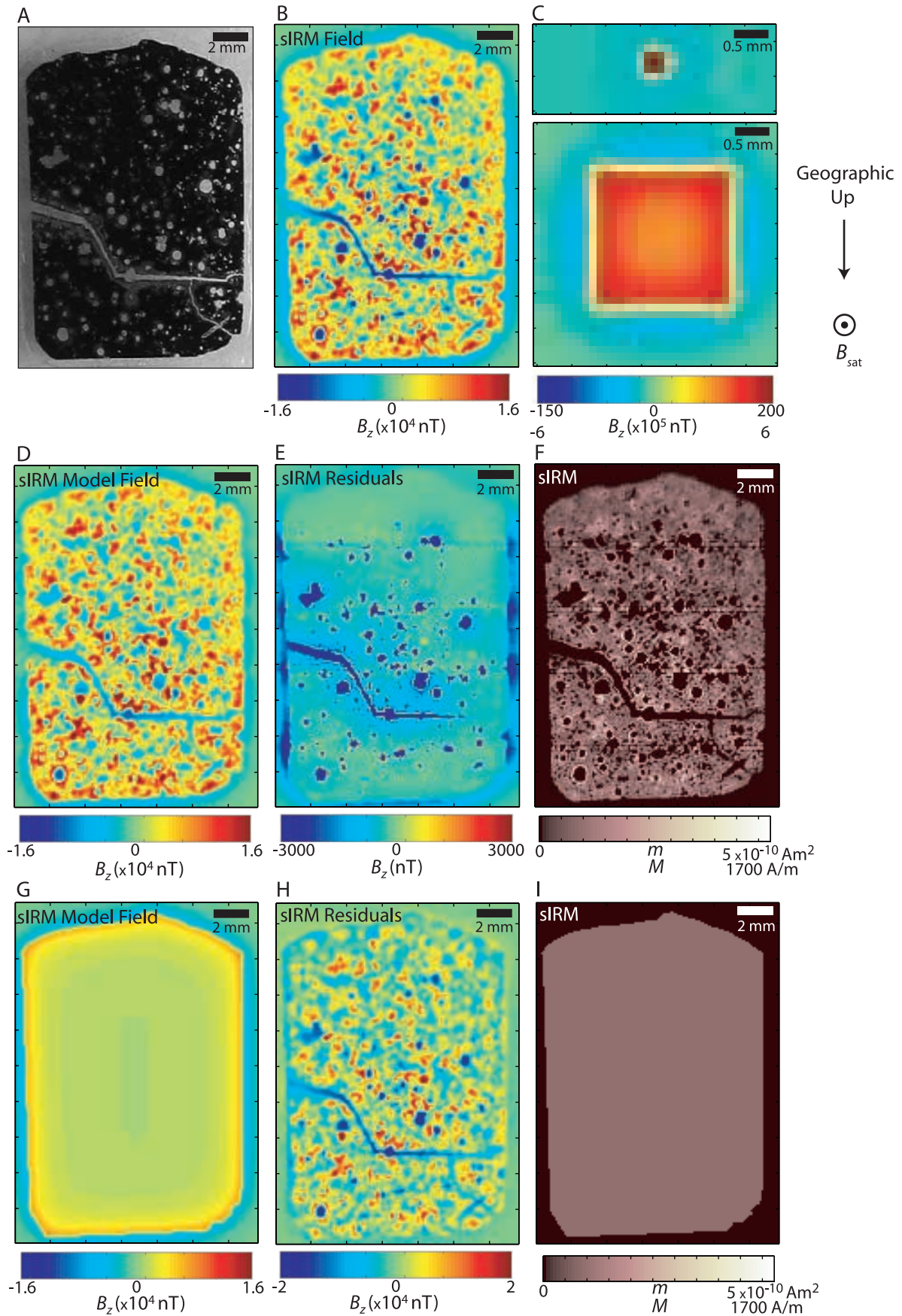


Figure 3

imum truncation threshold by conducting a series of trial fits on the sIRM data using various threshold distances  $r_0$  (Figure 5). For all scans we found that for  $r_0 \geq 6$  mm, the residual RMS showed negligible improvement while the total fit moment of the scan converged toward the sIRM measured with the 2G. We note that because the minimum acceptable value of  $r_0$  depends on the sample size and scanning geometry (for instance, it should grow with increasing horizontal sample size), it will need to be determined for each new sample analyzed with SQUID microscopy.

[46] The resulting uniform sIRM magnetization model field  $\mathbf{A}^\dagger \mathbf{d}^*$  (Figure 3g) (calculated from forward modeling the best fit solution (Table 2, Figures 2 and 3i)) has none of the zero-crossings and intensity variations seen in the data. This failure is manifested by highly spatially correlated, non-Gaussian residuals ( $\mathbf{A}^\dagger \mathbf{d}^* - \mathbf{b}$ ) (Figure 3h) whose intensities range up to several tens of thousands of nT, far exceeding our expected measurement errors. Using Appendix equation A1, the total errors (which should be dominated by position errors) should only be of order 100 nT.

[47] Nonetheless, there are some gross features about the solution which are qualitatively consistent with our expectations. A vertically magnetized dipole and a vertically magnetized plate both generate fields with positive  $B_z$  above the magnetized region and negative  $B_z$  (“demagnetizing field”) that symmetrically rings the edges of the magnetization (Figure 3c). The thin section edges in both the data (Figure 3b) and uniform solution (Figure 3g) show this approximately symmetric demagnetizing field (blue). In fact, the uniform sIRM fit is within the angular uncertainty of the 2G sIRM measurement (Figure 2). A second positive feature of the uniform solution is that its net moment (the sum of all dipoles in Figure 3i) is only 14% less than the 2G measurement (Table 2), although this is still outside the 5% uncertainty ( $\sim 10^{-7}$  Am<sup>2</sup>) of the 2G. The lower moment of the sIRM scan cannot be easily explained by viscous decay because it was found that after even several years of zero-field storage following the original 2G sIRM measurement the moment of the sample had decayed by only 3%.

[48] Because we created the sIRM using a spatially constant field, we might expect that a unidirectional solution

would provide a better description of its magnetization. We can hypothesize that like many other basalts, our sample might have only weak anisotropy of remanence and therefore would everywhere have magnetized parallel to the direction of the applied field. Indeed, the 2G sIRM measurement demonstrates that this is true of the net moment. All of this would predict that our sample *is* unidirectionally magnetized. To test this hypothesis, we solved for the best fit unidirectional solution (see section 3.5). Unlike for the uniform solution, we assigned a dipole to a location under every measurement (including those measurements off the edge of the thin section), for a total of  $Q = 25,976$  dipoles. As before, the dipoles were spaced at 100  $\mu\text{m}$  intervals. Because the applied field was oriented out of the plane of the thin section, the sIRM magnetization solution was required to have inclination  $i = -90^\circ$ . We then fit for the intensity of each dipole for a total of  $M = 25,976$  measurements and  $N = 25,976$  parameters. Computing a least squares fit for such a large Jacobian has memory and computational speed requirements that far outstrip our new desktop computer (a dual core 3.4 GHz Intel 64-bit processor with 4 GB of RAM and several hundred GB of virtual memory). Once again, we used sparse matrix techniques with  $r_0 = 6$  mm to estimate the Jacobian as  $\mathbf{A}^\dagger$  (Figure 5b) and the *lsqlin* routine, which reduced the computation time to several weeks. Even so, we unfortunately had to split the scan into four subsections and invert each separately, resulting in higher residuals at the subsection boundaries.

[49] The resulting residuals appear to be within our noise limits. It is difficult to make this statement definitive because we were unable to calculate the full (non-sparse) Jacobian, which meant that it was also not possible for us to exactly calculate the forward model (Figure 3d) and, as a result, the residuals (Figure 3e). The estimate of the forward model  $\mathbf{A}^\dagger \mathbf{d}^*$  therefore is of high quality only at locations that are close to dipole sources with substantial moments. Because the magnetization is concentrated in the groundmass (Figure 3f), the forward model is a poor estimate for locations above vesicles, cracks, and the thin section edges where the field is dominantly downward. This can be clearly seen from an examination of our estimated residuals,  $\mathbf{A}^\dagger \mathbf{d}^* - \mathbf{b}$ . Above the groundmass, the residuals (Figure 3e)

**Figure 4.** SQUID Microscope measurements and analysis field of the natural remanent magnetization (NRM) of basalt thin section. (a) Scan showing the vertical component of the NRM field  $\sim 190 \mu\text{m}$  above the sample. Same field of view as Figures 3a and 3b. (b) Top: Computed vertical component of the magnetic field  $190 \mu\text{m}$  above a dipole with same moment and orientation as the net NRM of the thin section (see Table 2). Colorbar ranges from  $-22$  to  $31 \times 10^5$  nT. Bottom: Computed vertical component of the magnetic field  $190 \mu\text{m}$  above a  $2 \text{ mm} \times 2 \text{ mm}$  plate with same total moment and orientation as the net NRM of the thin section. Colorbar ranges from  $-1.2$  to  $1.6 \times 10^5$  nT. (c) Orthographically projected directional plot showing the residual root mean square (RMS) for each unidirectional fit to the NRM as a function of assumed magnetization direction. Contour levels are spaced by units of 3 nT, with lowermost contour of 75 nT enclosing the direct 2G NRM measurement (star) (see Table 2). Highest contour is 159 nT at bottom. (d) Estimated forward model  $\mathbf{A}^\dagger \mathbf{d}^*$  of the NRM field using the best fit unidirectional magnetization solution (associated with the minimum residual RMS in (c)) with  $r_0 = 6$  mm. (e) Estimated residuals,  $\mathbf{A}^\dagger \mathbf{d}^* - \mathbf{b}$ , for the best fit unidirectional magnetization solution (difference between matrices imaged in (a) and (d)). (f) Best fit magnetic moments,  $\mathbf{d}^*$ , of each of 25,976 dipoles associated with the unidirectional magnetization model field in (d). This map also depicts the magnetization when normalized to sample volume ( $3 \times 10^{-13} \text{ m}^{-3}$  per dipole). (g) Estimated forward model,  $\mathbf{A}^\dagger \mathbf{d}$ , of the NRM field using the best fit uniform magnetization solution with  $r_0 = 6$  mm. (h) Residuals for the best fit uniform magnetization solution (difference between matrices imaged in (a) and (g)). (i) Best fit magnetic moments,  $\mathbf{d}^*$ , of each of 20,439 dipoles (and magnetization) associated with the uniform magnetization model field in (g). Scale bars in (a, d-i) are 2 mm and in (b) are 0.5 mm. Geographic up is toward the bottom of the page.

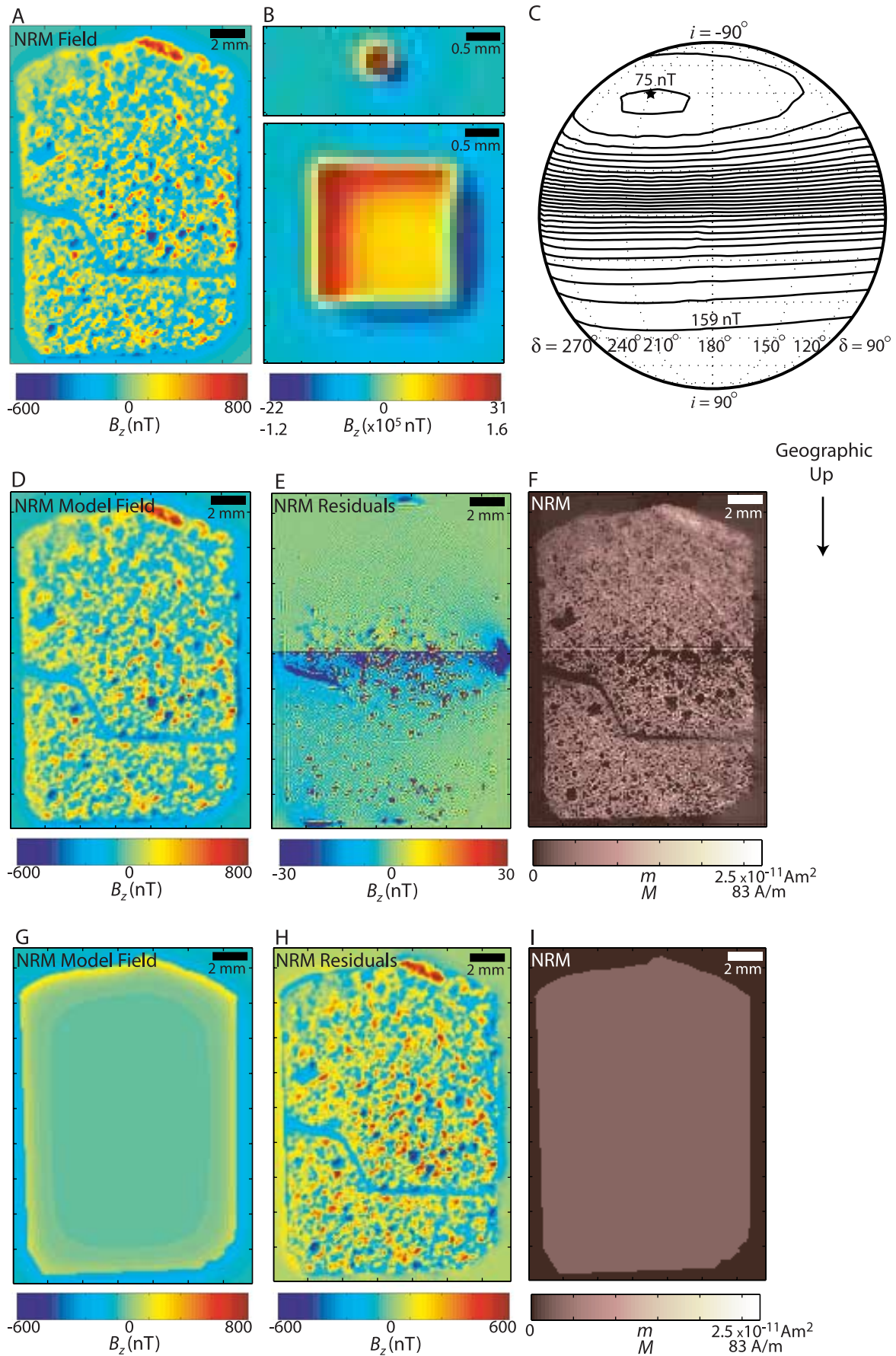
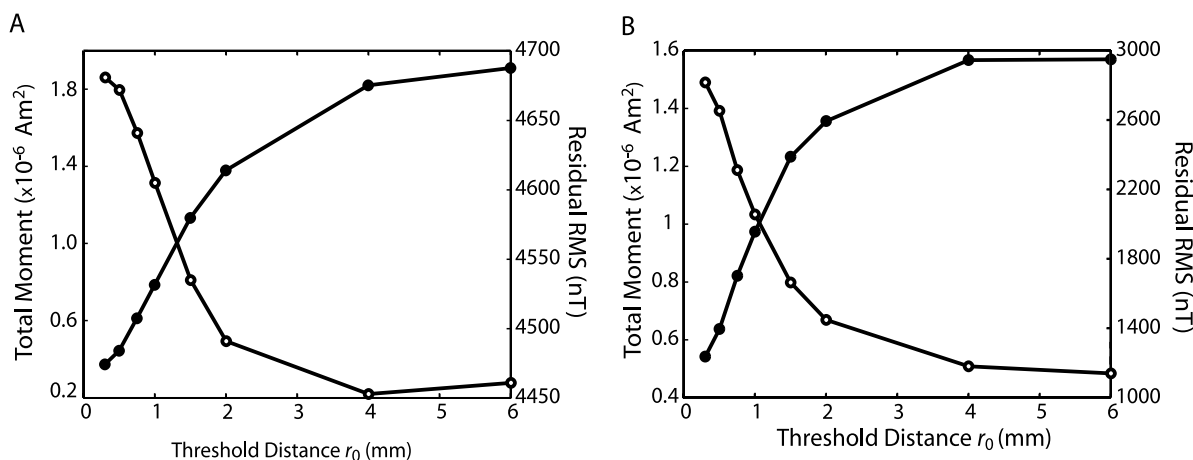


Figure 4



**Figure 5.** Effect of truncation of long range dipole interactions on the saturation isothermal remanent magnetization (sIRM) solutions. Shown are the residual root mean square (RMS) difference between the data and the forward model (open circles) and total dipole moment of the solution (closed circles), each plotted as a function of threshold distance  $r_0$  for both the (a) uniform and (b) unidirectional solutions. The total moments for  $r_0 = 6$  mm shown in (a) and (b) are given by the sum of the values in Figures 3e and 3h, respectively. The residual RMS for  $r_0 = 6$  mm shown in (a) and (b) are given by the square root of the ratio of the sum of the values in Figures 4d and 4g to the number of values. See Table 2.

are mostly uncorrelated and only 100–200 hundred nT, which is only several percent of the data values in these regions and at the level of the estimated position noise (Appendix A). On the other hand, above the vesicles and cracks and just outside the boundaries of the thin section, the residuals are spatially correlated and strongly negative. This is because the fields in these areas are not generated by nearby dipoles but rather are solely sourced from the aggregate demagnetizing fields of the groundmass dipoles throughout the entire thin section. Our truncation of the Jacobian means that the most of these demagnetizing fields are not taken into account when calculating the forward model estimate. A series of numerical experiments demonstrated this effect clearly: as we increased the value of  $r_0$  used to calculate the forward model, the demagnetizing fields in the void areas increased and the apparent residuals decreased (Figure 6).

[50] A second issue is that the 2G and the best fit SM unidirectional solution differ by 30% in total moment. This is far larger than the  $\sim 5\%$  uncertainty in the 2G moment magnitude. This discrepancy is likely a reflection of the misfit responsible for our residuals. Although the intensities of the residuals lead us to conclude that the dominant source of misfit is position noise (Appendix A), there are several other possible contributing sources. Some of the misfit could be the result of imprecise knowledge of the sample-to-sensor distance or undetected tilting or topography on the sample such that it is not all equidistant from the sensor. There may be some error introduced by truncation associated with conjugate gradient analysis. Finally, there also might be something subtly inaccurate about some of our other modeling assumptions (i.e., infinitely thin sample, infinitely small sensor, edge effects from splitting the scan into four subsections, or spacing and positioning of source dipoles). Any of these could contribute to the correlated residuals and discrepancy between the 2G and SM fit moments.

[51] In summary, a unidirectional magnetization fit is consistent with the SM sIRM data. The magnetization pattern indicates that indeed the magnetic sources are concentrated in the groundmass and not present in the vesicles, cracks or outside the thin section. Therefore the downward oriented (blue) fields observed above these voids and edges are in fact demagnetizing fields rather than the signature of downwardly oriented magnetization. The sIRM has an intensity of several hundred A/m in the basalt outside the vesicles and cracks (Figure 3f), in agreement with previous 2G measurements for bulk HSDP2 basalts [Kontny *et al.*, 2003]. The consistency of the solution with each these expected features provides further support for its accuracy as a description of the saturation remanent magnetization within the basalt.

#### 4.3.3.2. NRM Magnetic Field

[52] The NRM magnetic field (Figure 4a) is as complex as the sIRM field, again with highly variable intensity and numerous zero-crossings. Once again, regions with  $B_z > 0$  correspond almost exclusively to the dark groundmass, while those regions with  $B_z < 0$  correspond to vesicles, cracks and the thin section edges. However, there are also significant differences between the NRM and sIRM scans. First, the NRM field is about two orders of magnitude less intense, as expected for a VRM formed in a  $50 \mu\text{T}$  field that is more than 1000 times weaker than the laboratory field that generated the sIRM. Secondly, the demagnetizing field does not symmetrically ring the thin section, but is much stronger on the bottom and right edges. This demagnetizing field is roughly what one might expect from a dipole or plate magnetized in a direction with negative inclination and declination toward the upper left (Figure 4b). This just happens to be the same direction as the 2G NRM measurement.

[53] Given that we found that even the sIRM was not uniform, it would certainly be surprising if the NRM were uniform. Indeed, a uniform magnetization fit (Figures 4g and 4i), while giving a net moment intensity very close to

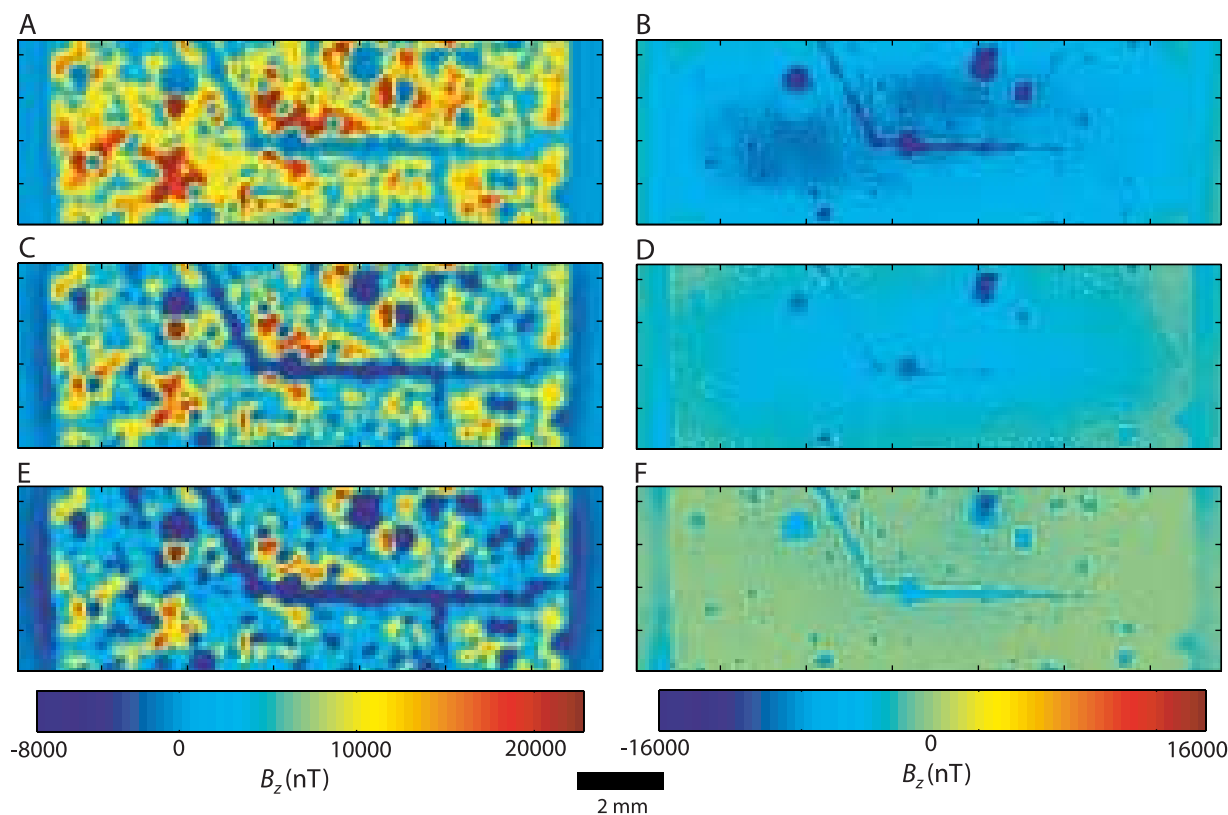


**Figure 6.** Various estimates of the forward model,  $\mathbf{A}^\dagger \mathbf{d}^*$ , and residuals,  $\mathbf{A}^\dagger \mathbf{d}^* - \mathbf{b}$ , for the saturation isothermal remanent magnetization (sIRM) field. All estimates here were computed using a solution  $\mathbf{d}^*$  that was originally computed from a Jacobian  $\mathbf{A}^\dagger$  estimated with  $r_0 = 6$  mm. (a) Estimated forward model for  $r_0 = 0.5$  mm. (b) Estimated residuals associated with forward model in (a). (c) Estimated forward model for  $r_0 = 1$  mm. (d) Estimated residuals associated with forward model in (c). (e) Estimated forward model for  $r_0 = 8$  mm. (f) Estimated residuals associated with forward model in (e).

that measured with the 2G (Table 2), has a direction that is  $\sim 60^\circ$  divergent and has residuals (Figure 4h) that are highly correlated and far exceed our measurement uncertainty of 10 nT.

[54] Because the basalt sample is young (has existed during only the current polarity chron), unbrecciated, relatively unaltered, and has a compositionally homogenous groundmass at the centimeter scale, we might also predict that its NRM would also be unidirectional to within our measurement uncertainties. Because its NRM is actually a VRM, the NRM is the vector sum of components which could be multidirectional due to secular variation on a timescale shorter than the lifetime of its VRM. However, if the distribution of titanomagnetite crystals in the groundmass is homogenous on the scale of our spatial resolution, then a unidirectional solution would still be successful at fitting the data. This is another hypothesis we can test by fitting for a unidirectional magnetization.

[55] In principle, we do not *a priori* know the NRM direction unless we use the 2G NRM measurement as a constraint. We chose not to do so because by allowing the fits to select a best fit direction, we could test the unidirectional hypothesis by not only the standard method of examining the residuals but by an additional criterion: the agreement in net direction with the known (2G) value. Therefore the magnetization was not specified for our unidirectional NRM fits.

[56] Rather, the unit sphere was uniformly tiled following [Rakhmanov *et al.*, 1994; Saff and Kuijlaars, 1997] and a best fit intensity solution was separately obtained for each orientation direction. The best fit direction is that with the lowest residual RMS, and the best fit intensity is the intensity solution associated with this direction [Parker, 1991]. Because unidirectional fits can exhibit numerous local minima on the unit sphere [Parker, 1991], it is important for the angular search grid to be fairly fine. All told, we obtained a unidirectional solution for 666 search directions. Because even a single such fit using sparse matrix methods with  $r_0 = 6$  mm would require a week of time on our computer (i.e., the sIRM fit), we had to make further approximations to make the calculations tractable. Instead of using one dipole for each of the 25,976 measurements, we began by only placing dipoles at locations where data values  $B_z$  exceeded 150 nT. This reduced the number of dipoles to 8,749 and restricted their location to within the groundmass and outside the vesicles and cracks. This shortcut is justified for two reasons: petrographic data show that the vesicles and crack areas are nonmagnetic, and the sIRM magnetization unidirectional solution (Figure 3f) indicates that there are essentially no magnetic carriers in these same locations.

[57] The results (Figure 4c) showed a single global minimum with inclination  $i = -43^\circ$  and clockwise declination  $\delta = 212^\circ$  that is very close to the 2G NRM measure-

ment as well as the borehole fluxgate inclination (Figure 2). This corresponds to an inclination of  $i' = 22^\circ$  in geographic coordinates, which is roughly what one would expect for a sample from Hawaii with a VRM acquired in the Earth's present field (the actual inclination at Mauna Kea today is  $37^\circ$ ). However, the net moment intensity for this solution was about half the 2G value (Table 2). Because we suspected this discrepancy was the result of our computational shortcut of artificially reducing the number of dipoles, we conducted a second fit using 25,976 dipoles (one for each measurement) but restricting the orientation to the previously identified best fit-direction. To alleviate memory and computational demands, the scan was divided into two subsections and each section was fit separately. The resulting solution was four times more intense than the previous solution and in fact 28% more intense than the 2G measurement. Again, this disagreement in total moment must be at least partly a result of position noise, and it could potentially be eliminated by improving the SM hardware or bounding the SM solution norm to within the uncertainties of the 2G moment magnitude. For the same reasons stated during the discussion about the NRM fitting, it is possible that part of this misfit is a result of our modeling assumptions or computational shortcuts. Away from the boundary separating the two subsections, the residuals (Figure 4e) are mostly uncorrelated and of order 10 nT, close to our expected measurement noise.

[58] We would like an estimate of the uncertainty on the best-direction for the unidirectional solution. Parker [Parker, 1991] approached this by setting the uncertainty to that contour on the residual plot corresponding to the measurement uncertainty. However, our residual plot is only an estimate of the true residuals because of the reduced number of dipoles with respect to our final solution. Worse, even the residuals for our final solution with the full number of dipoles (Figure 4e) are themselves an estimate because of the truncation of the Jacobian (see above). Therefore we were unable to place a bound on the accuracy of the best fit direction except to note again its superb agreement with the 2G measurement.

[59] The NRM unidirectional fit corresponds to a magnetization of  $\sim 10\text{--}20$  A/m in the basalt outside the vesicles and cracks (Figure 4f), consistent with what has been previously measured for HSDP basalts [Kontny *et al.*, 2003]. As with the sIRM, the magnetization is concentrated in the groundmass, such that the fields with negative  $B_z$  above the voids, cracks, and section edges are demagnetizing fields rather than the result of oppositely oriented magnetization. Again, the consistency of the solution with each these expected features provides additional support for the use of a unidirectional model for the NRM.

#### 4.3.4. Uniqueness of Unidirectional Solutions

[60] We have argued that the magnetization solutions retrieved from the sIRM and NRM data are within the uncertainties of our measurements. Therefore our data are consistent with the hypothesis that the sIRM and NRM are unidirectional throughout the basalt. As pointed out by Parker, there is no guarantee that a nonnegative unidirectional magnetization solution will fit a particular magnetic field data set (note that the same is *not* true for unidirectional solutions without the nonnegativity constraint). Therefore using SQUID microscopy we have indeed

learned something unique about the magnetization within the basalt that would not have been knowable from the 2G data alone.

[61] We have already addressed the uniqueness of the magnetization orientation in section 4.3.3. However, for a given orientation, how unstable is the intensity pattern of the magnetization solution? As is true for essentially all iterative least squares methods, we found that the nature of the solution depends on the number of iterations. In particular, it has often been observed for conjugate gradient methods that as number of iterations is increased, the residual RMS drops while the solution norm (or other measures of instability) increases [Hansen, 1998]. Therefore conjugate gradient methods are inherently regularizing, with the number of iterations serving as a regularization parameter.

[62] One would not expect our unidirectional solutions to be highly unstable because the nonnegativity requirement prevents the solution from having the high-frequency, high-amplitude positive and negative oscillations that are typical of less constrained magnetization inversions [Parker, 1994]. To confirm this, for a subset of the sIRM data (lower left corner of Figure 6a) we computed a series of solutions by varying the number maximum number of iterations. For each solution we calculated the residual RMS as a measure of misfit and three different measures of solution instability: the Euclidean norm  $\|\mathbf{d}^*\|$ , standard deviation  $\text{stdev}(\mathbf{d}^*)$ , and the summed gradient  $\sum \|\nabla m\|$ . We found that as the number of iterations increased, the residual RMS decreased while the solution became slowly less smooth, particularly around the edges of the magnetization (compare Figures 7a, 7b, 7c). This decrease in smoothness is reflected in a gradual increase in the standard deviation and the summed gradient (Figure 7d). This functional behavior is similar in shape but *far* smaller in magnitude than L-curves typical of ill-posed problems [Hansen, 1998]. The solution which best fulfills the tradeoff between smoothness and residual is that pictured in Figure 7b. Interestingly, although the solution norm does not show this same L-curve behavior, its minimum occurs just at the same solution. Therefore we have three different indicators that this solution is optimal. Because the instability indicators do not vary much as a function of iteration number, we can see that the unidirectional intensity solution for the sIRM is reasonably smooth.

#### 4.3.5. Future Improvements

[63] There are at least four simple ways to improve our future magnetization inversions. The first is to modify the SM hardware to reduce the position noise. The second is to require the SM solution to have a total moment within the uncertainties of the 2G moment (*Isqclin* has the capability to put upper and lower bounds on  $\mathbf{d}$ ). We chose not to impose such constraints on  $\mathbf{d}$  here since our intention was not to obtain the most realistic fit but rather to demonstrate that SM data are validated by 2G measurements. The third is to constrain our space domain solutions using frequency domain inversions. When conducted using field data that have been measured on both sides of a thin section, frequency domain techniques can *uniquely* calculate the vertical component of the magnetization per unit area [Egli and Heller, 2000]. Our unidirectional space domain magnetization solutions could then be forced to have  $z$ -components that match those mandated by the frequency

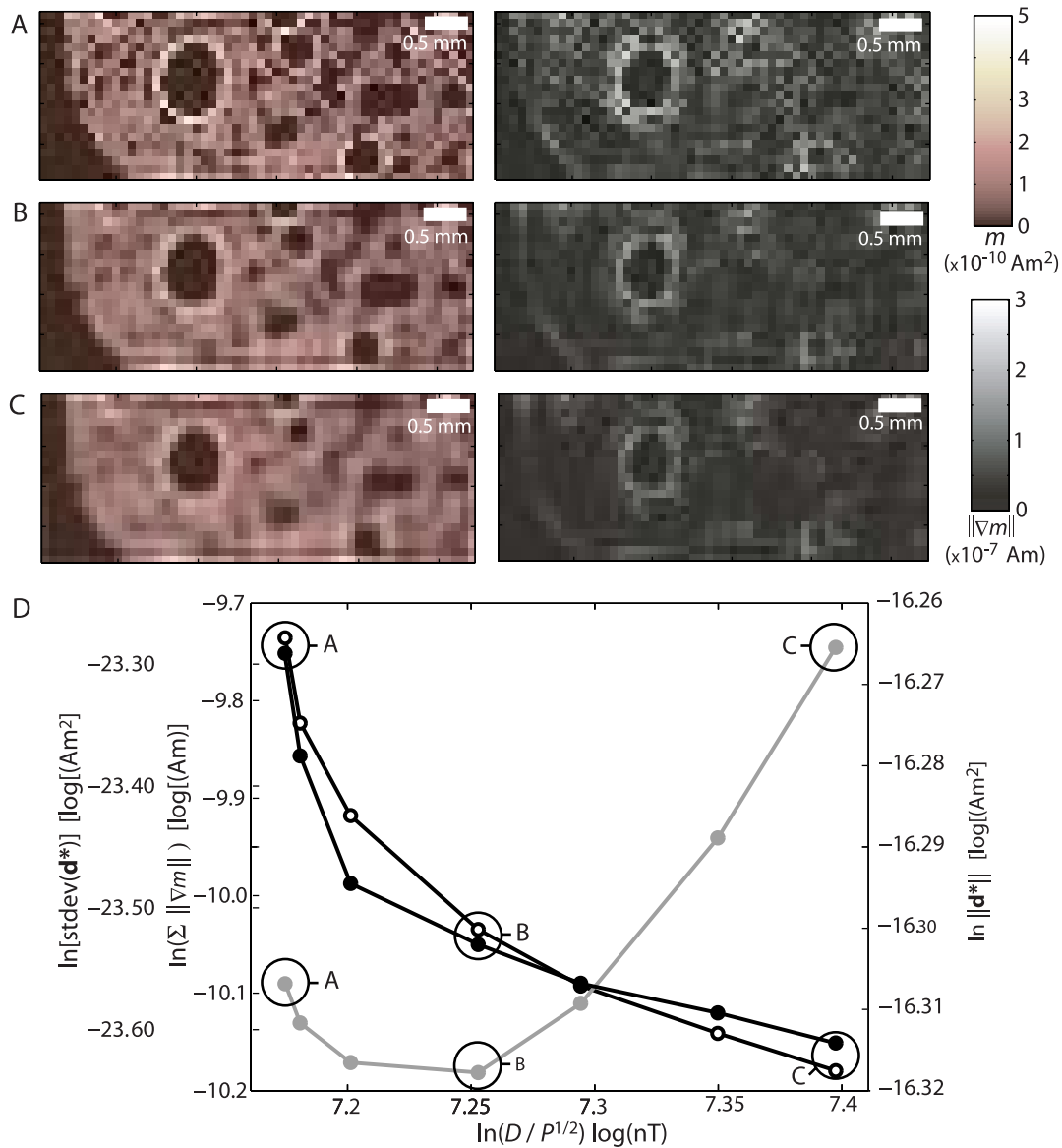


**Figure 7.** The effect of the maximum number iterations on the stability of the saturation isothermal remanent magnetization (sIRM) unidirectional magnetization inversion. All estimates  $\mathbf{d}^*$  here were computed from a subset of the sIRM scan (bottom left portion of Figure 3b) using a Jacobian  $\mathbf{A}^\dagger$  estimated with  $r_0 = 6$  mm. (a) Left: Best fit moments,  $\mathbf{d}^*$ , of each dipole for solution with residual RMS = 1306 nT. Right: Euclidean norm of the gradient of this solution,  $\|\nabla m\|$ . This is the solution labeled “A” in 7d. (b) Best fit moments,  $\mathbf{d}^*$ , of each dipole for solution with residual RMS = 1412 nT. Right: Euclidean norm of the gradient of this solution,  $\|\nabla m\|$ . This is the solution labeled “B” in 7d. The L-curve and minimum norm analysis in 7d indicates this is the optimal solution. (c) Left: Best fit moments,  $\mathbf{d}^*$ , of each dipole for solution with residual RMS = 1632 nT. Right: Euclidean norm of the gradient of this solution,  $\|\nabla m\|$ . This is the solution labeled “C” in 7d. (d) The Euclidean norm  $\|\mathbf{d}^*\|$  (gray circles), standard deviation  $\text{stdev}(\mathbf{d}^*)$  (solid black symbols), and the summed gradient  $\sum \|\nabla m\|$  [defined as the sum of all values in each left frame in (a–c)] (open black symbols) for various solutions  $\mathbf{d}^*$  as a function of residual RMS. The solutions pictured in (a–c) are lettered.

inversions. Finally, we can optimize the solution misfit to modeling parameters like dipole spacing, sample thickness, and sample tilt.

### 5. Conclusions

[64] The purpose of this work is to demonstrate how SQUID microscopy can make high-resolution measure-

ments previously inaccessible to SQUID-based rock magnetometers and how these data can be used to learn something fundamentally new and of value to paleomagnetism and geoscience. We have shown that within the uncertainty of our measurements, two lunar spherules appear as dipolar point sources to the SQUID Microscope. One of these samples has a moment that is too weak to be detected with a 2G Enterprises Superconducting Rock

Magnetometer. In fact, our SQUID Microscope measurements of the NRM field of Spherule 2 make its NRM probably the weakest ever to have been detected in the history of paleomagnetism. In contrast, our SQUID Microscope study of the Hawaiian basalt thin section is probably the highest resolution quantitative paleomagnetic study of natural remanent magnetization to date. That our measurements are in agreement with data from a variety of other instruments—a 2G SRM, borehole fluxgate magnetometer, and a variety of rock magnetic and petrographic techniques—in turn validates our technique.

[65] We have also shown that not only can we map the magnetic fields of the basalt, we can use these maps to learn a number of things about the interior structure of its magnetization which cannot be learned from moment magnetometry measurements alone:

[66] 1. Neither the basalt's NRM nor sIRM are spatially uniform. This is because uniform solutions have spatially correlated residuals which exceed our noise level, and (for the NRM) do not match direct measurements with a 2G.

[67] 2. Our data are consistent with the hypothesis that the basalt's NRM and sIRM are unidirectional throughout the thin section. Approximate unidirectionality is the expected solution because the sample has existed during a single polarity chron and its magnetic minerals are predominantly primary. Our data support this expectation.

[68] 3. The best fit unidirectional magnetization solution indicates that magnetic sources lie inside the groundmass and not in vesicles, cracks, and the quartz mount. This is consistent with petrographic data which indicate that the main magnetic mineral, titanomagnetite, is concentrated in the groundmass.

[69] 4. A vertical unidirectional fit to the sIRM matches the bulk 2G measurements. Therefore the basalt has at most very weak anisotropy of remanence throughout. This is consistent with previous anisotropy of remanence studies of Hawaiian basalts.

## Appendix A: Sources of Noise

[70] The SQUID Microscope is sufficiently shielded such that environmental magnetic noise does not exceed our measurement noise. Our limiting sensitivity is therefore determined by measurement noise which has two major components: intrinsic sensor noise and position noise. We discuss each in turn.

[71] *Sensor noise.* SQUIDs measure changes in magnetic field with respect to an arbitrary zero point. To obtain absolute field values, we set the SQUID Microscope's output voltage to zero at the start of every scanning line where the sensor is in a region of approximately zero field (typically attained several mm away from the sample edge). Because a single line scan across a 25-mm diameter thin section typically takes 10–100 s, this means that the minimum noise frequency that could affect the measurements is  $\sim 0.1$ – $0.01$  Hz. The maximum frequency is set by the scanning rate (typically a few data points per sec). Therefore the noise range of interest to geological applications of SQUID microscopy is between  $\sim 0.01$  and  $< \sim 10$  Hz. Integrated over 0.01–10 Hz, our low- $T_c$  SQUID Microscope equipped with a 80  $\mu\text{m}$  washer sensor has a sensitivity to a spatially uniform field of approximately

$10^{-2}$  nT when operated at its most sensitive dynamic range setting. When this sensor is operated at a distance of 100  $\mu\text{m}$ , this field sensitivity translates to an extraordinary dipole moment sensitivity of better than  $10^{-15}$  Am<sup>2</sup>, more than three orders of magnitude better than the best superconducting moment magnetometers.

[72] *Position noise.* Aside from the sensor noise, there is another source of noise which has a significant effect on the quality of our data. This is position noise [Lee *et al.*, 2004]. It originates from imperfections in the sample positioning system (motor jitter, encoder errors, and mechanical hysteresis associated with backlash of the scanning stage), which translates into imprecise knowledge of the horizontal position of the sample with respect to the sensor. Position noise is insidious in that it scales with the intensity of the measurement, making it difficult to detect while degrading the most intense measurements in an image. This is unfortunate because the most intense measurements also dominate the least squares analyses.

[73] Because position noise has only been quantitatively studied recently, we have yet to systematically characterize its effects on SQUID Microscope data. Nevertheless, our experience suggests that our horizontal positional accuracy is currently  $\sim 1$ – $10$   $\mu\text{m}$ . Lee *et al.* [2004] demonstrate that for a dipole moment  $m$ , sample-to-sensor distance  $h$ , and permeability of free space  $\mu_0$ , the field noise originating from horizontal positioning errors with standard deviation  $\sigma_x$ :

$$\sigma_{B_z} = \frac{1875\mu_0 m}{1372\sqrt{35}\pi h^4} \sigma_x \quad (\text{A1})$$

Note that although (A1) was derived under the assumption of uncorrelated position noise, in fact position errors will very likely depend on the spatial location of the sensor. Furthermore, the Lee *et al.* analysis is for a single scanning axis, such that the position noise in our two-dimensional scanning configuration will be even worse than that implied by (A1). Therefore we expect it provides a lower limit on our position errors.

[74] Using (A1) and the moments listed in Table 1, we see that position noise should dominate the sIRM scans of both spherules as well as the NRM scan of Spherule 1. For the Spherule 2 NRM scan, the position noise should be comparable to the sensor noise, which is consistent with the relatively much lower residuals from the fits to this scan. Inspection of the typical moment magnitudes in Figures 3f and 4f demonstrates that it should also dominate both the NRM and sIRM measurements of the basalt nearly everywhere inside the boundaries of the thin section.

[75] Because our spring-loaded mechanism pushes the sample up against the sapphire window, the vertical distance between our sensor and sample,  $h$ , does not undergo the relatively high frequency jitter that the horizontal position experiences during scanning. We measure this distance by scanning a wire of known current (typically several mA) and fitting the field data for  $h$  [Baudenbacher *et al.*, 2002b]. We have recently conducted a series of numerical experiments on simulated SM scans of wire with simulated horizontal position errors of 1–10  $\mu\text{m}$ . The experiments demonstrated that the uncertainty in our estimate of  $h$ , which should originate mainly from horizontal position

errors, is less than 0.1%. Therefore imprecise knowledge of  $h$  is likely not the dominant noise source for scans of planar samples.

[76] **Acknowledgments.** We thank R. Bennett-Calorio and M. Pendleton for administrative assistance, J. Wikswo for open access to the VIIBRE facilities for the past seven years, C. Dwyer and K. McBride for assistance with the magnetic measurements of the spherules, E. Staveling for sharing his unpublished HSDP2 borehole magnetic data, T. Scheider for helpful discussions about inverse theory, I. Ceraj for introducing us to the world of 64 bit computing, N. Gitahi and C. Seaman for assistance with sampling the HSDP core, and the HSDP team for access to its valuable samples. B. Weiss and F. Baudenbacher thank the NSF Geophysics, NSF Instrumentation and Facilities, NASA Mars Fundamental Research, and the NASA Planetary Major Equipment Programs.

## References

- Aster, R. C., B. Borchers, and C. H. Thurber (2005), *Parameter Estimation and Inverse Problems*, 301 pp., Elsevier Academic Press, Burlington.
- Baker, M. B., S. Alves, and E. M. Stolper (1996), Petrology and petrography of the Hawaii Scientific Drilling Project lavas: Inferences from olivine phenocryst abundances and compositions, *J. Geophys. Res.*, *101*, 11,715–11,727.
- Baudenbacher, F. J., N. T. Peters, J. P. Wikswo, and M. Radparvar (1998), High resolution LTS-SQUID magnetometer, *Bull. Am. Phys. Soc.*, *43*, 1626.
- Baudenbacher, F. J., N. T. Peters, and J. P. Wikswo (2002a), High resolution low-temperature superconductivity superconducting quantum interference device microscope for imaging magnetic fields of samples at room temperatures, *Rev. Sci. Instrum.*, *73*, 1247–1254.
- Baudenbacher, F., N. T. Peters, P. Baudenbacher, and J. P. Wikswo (2002b), High resolution imaging of biomagnetic fields generated by action currents in cardiac tissue using a LTS-SQUID microscope, *Physica C*, *368*, 24–31.
- Baudenbacher, F., L. E. Fong, J. R. Holzer, and M. Radparvar (2003), Monolithic low-transition-temperature superconducting magnetometers for high resolution imaging magnetic fields of room temperature samples, *Appl. Phys. Lett.*, *82*, 3487–3489.
- Blakely, R. J. (1996), *Potential Theory in Gravity and Magnetic Applications*, 441 pp., Cambridge Univ. Press, New York.
- Bott, M. H. P., and M. A. Hutton (1970), Limitations on the resolution possible in the direct interpretation of marine magnetic anomalies, *Earth Planet. Sci. Lett.*, *8*, 317–319.
- Braginski, A., and J. Clarke (2004), Introduction, in *The SQUID Handbook*, edited by J. Clarke and A. I. Braginski, pp. 1–28, Wiley-VCH, Weinheim.
- Cavarretta, G., A. Coradini, R. Funicello, M. Fulchignoni, A. Taddeucci, and R. Trigila (1972), Glassy particles in Apollo 14 soil 14163,88: Peculiarities and genetic considerations, *Proc. Lunar Sci. Conf.*, *3*, 1085–1094.
- Chatrathorn, S., E. F. Fleet, and F. C. Wellstood (2002), Relationship between spatial resolution and noise in scanning superconducting quantum interference device microscopy, *J. Appl. Phys.*, *92*, 4731–4740.
- Clem, T. R., C. P. Foley, and M. N. Keene (2006), SQUIDS for geophysical survey and magnetic anomaly detection, in *The SQUID Handbook*, edited by J. Clarke and A. I. Braginski, pp. 481–543, Wiley-VCH, Weinheim.
- Cochran, A., G. B. Donaldson, S. Evanson, and R. J. P. Bain (1993), First-generation SQUID-based nondestructive testing system, *IEEE Proc. A*, *140*, 113–120.
- Culler, T. S., T. A. Becker, R. A. Muller, and P. R. Renne (2000), Lunar impact history from  $^{40}\text{Ar}/^{39}\text{Ar}$  dating of glass spherules, *Science*, *287*, 1785–1788.
- Dampney, C. N. G. (1969), The equivalent source technique, *Geophysics*, *34*, 39–53.
- Dechert, J., M. Mueck, and C. Heider (1999), A scanning SQUID microscope for samples at room temperature, *IEEE Trans. Appl. Supercond.*, *9*, 4111–4114.
- DePaolo, D. J., E. M. Stolper, D. M. Thomas, and M. O. Garcia (1999), Hawaii Scientific Drilling Project: Core logs and summarizing data, Pasadena.
- Egli, R., and F. Heller (2000), High-resolution imaging using a high-Tc superconducting quantum interference device (SQUID) magnetometer, *J. Geophys. Res.*, *105*, 25,709–25,727.
- Emilia, D. A. (1973), Equivalent sources used as an analytic base for processing total magnetic field profiles, *Geophysics*, *38*, 339–348.
- Emilia, D. A., and R. L. Massey (1974), Magnetization estimation for nonuniformly magnetized seamounts, *Geophysics*, *39*, 223–231.
- Fagaly, R. (2006), Superconducting quantum interference device instruments and applications, *Rev. Sci. Instrum.*, *77*, 101101.
- Fleet, E. F., S. Chatrathorn, F. C. Wellstood, and C. Eylem (2001), Determination of magnetic properties using a room-temperature scanning SQUID microscope, *IEEE Trans. Appl. Supercond.*, *11*, 1180–1183.
- Fong, L. E., J. R. Holzer, K. K. McBride, E. A. Lima, F. Baudenbacher, and M. Radparvar (2004), Multiloop low-transition-temperature SQUID sensor for imaging biomagnetic fields with submillimeter resolution, *Appl. Phys. Lett.*, *84*, 3190–3193.
- Fong, L. E., J. R. Holzer, K. K. McBride, E. A. Lima, and F. Baudenbacher (2005), High resolution room-temperature sample scanning superconducting interference device microscope configurable for geological and biomagnetic applications, *Rev. Sci. Instrum.*, *76*, 053703.
- Fuller, M., and S. M. Cisowski (1987), Lunar paleomagnetism, in *Geomagnetism*, edited by J. A. Jacobs, pp. 307–455, Academic Press, Orlando.
- Fuller, M., W. S. Goree, and W. L. Goodman (1985), An introduction to the use of SQUID magnetometers in biomagnetism, in *Magnetite Biomineralization and Magnetoreception in Organisms: A New Biomagnetism*, edited by J. L. Kirschvink et al., pp. 103–151, Plenum Press, New York.
- Gattacceca, J., M. Boustie, B. P. Weiss, P. Rochette, E. A. Lima, L. E. Fong, and F. J. Baudenbacher (2006), Investigating impact demagnetization through laser impacts and SQUID microscopy, *Geology*, *34*, 333–336.
- Gee, J., H. Staudigel, and L. Tauxe (1989), Contribution of induced magnetization to magnetization of seamounts, *Nature*, *342*, 170–173.
- Hansen, P. C. (1998), *Rank-Deficient and Discrete Ill-Posed Problems: Numerical Aspects of Linear Inversion*, 247 pp., Society for Industrial and Applied Mathematics, Philadelphia.
- Hansen, P. C. (2001), *Regularization Tools: A Matlab Package for Analysis and Solution of Discrete Ill-Posed Problems, Version 3.1 for Matlab 6.0*, 109 pp., available online at <http://www.imm.dtu.dk/~pch>.
- Hildebrand, J. A., and R. L. Parker (1987), Paleomagnetism of Cretaceous Pacific seamounts revisited, *J. Geophys. Res.*, *92*, 12,695–12,712.
- Judge, G. G., R. C. Hill, W. E. Griffiths, H. Lutkepohl, and T.-C. Lee (1988), *Introduction to the Theory and Practice of Econometrics*, Wiley, New York.
- Ketchen, M. B., J. R. Kirtley, and M. Bhushan (1997), Miniature vector magnetometer for scanning SQUID microscopy, *IEEE Trans. Appl. Supercond.*, *7*, 3139–3142.
- Kirschvink, J. L. (1992), Uniform magnetic fields and double-wrapped coil systems: Improved techniques for the design of bioelectromagnetic experiments, *Bioelectromagnetics*, *13*, 401–411.
- Kirtley, J. R., and J. P. Wikswo (1999), Scanning SQUID microscopy, *Annu. Rev. Mater. Sci.*, *29*, 117–148.
- Kono, M. (1977), Paleomagnetism of DSDP Leg 55 basalts and implications for the tectonics of the Pacific Plate, *Initial Rep. Deep Sea Drill. Project*, *55*, 737–758.
- Kontny, A., C. Vahle, and H. de Wall (2003), Characteristic magnetic behavior of subaerial and submarine lava units from the Hawaiian Scientific Drilling Project (HDSP-2), *Geochem. Geophys. Geosyst.*, *4*(2), 8703, doi:10.1029/2002GC000304.
- Krasa, D. (2002), Partial self-reversal of the NRM in basalts: Identifying the responsible mineral phases, *IRM Quarterly*, *12*, 3–4.
- Kress, R., L. Kuhn, and R. Potthast (2002), Reconstruction of a current distribution from its magnetic field, *Inverse Problems*, *18*, 1127–1146.
- Labotka, T. C., M. J. Kempa, C. White, J. J. Papike, and J. C. Laul (1980), The lunar regolith: Comparative petrology of the Apollo sites, *Proc Lunar Planet. Sci. Conf.*, *11*, 1285–1305.
- Langel, R. A., and W. J. Hinze (1998), *The Magnetic Field of the Earth's Lithosphere*, 429 pp., Cambridge Univ. Press, Cambridge.
- Langel, R. A., E. V. Slud, and P. J. Smith (1984), Reduction of satellite magnetic anomaly data, *J. Geophys.*, *54*, 207–212.
- Lee, T. S., E. Dantsker, and J. Clarke (1996), High-transition temperature superconducting quantum interference device microscope, *Rev. Sci. Instrum.*, *67*, 4208–4215.
- Lee, S.-Y., J. Mathews, and F. C. Wellstood (2004), Position noise in scanning superconducting quantum interference device microscopy, *Appl. Phys. Lett.*, *84*, 5001–5003.
- Levine, J., T. A. Becker, R. A. Muller, and P. R. Renne (2005),  $^{40}\text{Ar}/^{39}\text{Ar}$  dating of Apollo 12 impact spherules, *Geophys. Res. Lett.*, *32*, L15201, doi:10.1029/2005GL022874.
- Lima, E. A., A. Irimia, and J. P. Wikswo (2006), The magnetic inverse problem, in *The SQUID Handbook*, edited by J. Clarke and A. I. Braginski, pp. 139–267, Wiley-VCH, Weinheim.
- Mayhew, M. A. (1979), Inversion of satellite magnetic anomaly data, *J. Geophys.*, *45*, 119–128.
- Mayhew, M. A. (1982), An equivalent layer magnetization model for the United States derived from satellite altitude magnetic anomalies, *J. Geophys. Res.*, *87*, 4837–4845.
- Mayhew, M. A., and S. C. Galliher (1982), An equivalent layer magnetization model for the United States derived from Magsat data, *Geophys. Res. Lett.*, *9*, 311–313.
- McNutt, M. (1986), Nonuniform magnetization of seamounts: A least squares approach, *J. Geophys. Res.*, *91*, 3686–3700.

- Nicolosi, I., I. Blanco-Montenegro, A. Pignatelli, and M. Chiappini (2006), Estimating the magnetization direction of crustal structures by means of an equivalent source algorithm, *Phys. Earth Planet. Inter.*, *155*, 163–169.
- Nowaczyk, N. R., H.-U. Worm, A. Knecht, and J. H. Hinken (1998), Imaging distribution patterns of magnetic minerals by a novel high-Tc-SQUID-based field distribution measuring system: Applications to Permian sediments, *Geophys. J. Int.*, *132*, 721–726.
- Parker, R. L. (1971), The determination of seamount magnetism, *Geophys. J. R. Astron. Soc.*, *24*, 321–324.
- Parker, R. L. (1977), Understanding inverse theory, *Annu. Rev. Earth Planet. Sci.*, *5*, 35–64.
- Parker, R. L. (1988), A statistical theory of seamount magnetism, *J. Geophys. Res.*, *93*, 3105–3115.
- Parker, R. L. (1991), A theory of ideal bodies for seamount magnetism, *J. Geophys. Res.*, *96*, 16,101–16,112.
- Parker, R. L. (1994), *Geophysical Inverse Theory*, 386 pp., Princeton Univ. Press, Princeton.
- Parker, R. L., L. Shure, and J. A. Hildebrand (1987), The application of inverse theory to seamount magnetism, *Rev. Geophys.*, *25*, 17–40.
- Press, W. H., S. A. Teukolsky, W. T. Vetterling, and B. P. Flannery (1992), *Numerical Recipes in Fortran 77: The Art of Scientific Computing*, 933 pp., Cambridge Univ. Press, Cambridge.
- Purucker, M. E., T. J. Sabaka, and R. A. Langel (1996), Conjugate gradient analysis: A new tool for studying satellite magnetic data sets, *Geophys. Res. Lett.*, *23*, 507–510.
- Rakhmanov, E. A., E. B. Saff, and Y. M. Zhou (1994), Minimal discrete energy on the sphere, *Math. Res. Lett.*, *1*, 647–662.
- Roth, B. J., N. G. Sepulveda, and J. P. Wiksw Jr. (1989), Using a magnetometer to image a two-dimensional current distribution, *J. Appl. Phys.*, *65*, 361–372.
- Saff, E. B., and A. B. J. Kuijlaars (1997), Distributing many points on a sphere, *The Mathematical Intelligencer*, *19*, 5–11.
- Sepulveda, N. G., I. M. Thomas, and J. P. Wiksw (1994), Magnetic susceptibility tomography for three-dimensional imaging of diamagnetic and paramagnetic objects, *IEEE Trans. Mag.*, *30*, 5062–5069.
- Sharp, W. D., and P. R. Renne (2005), The  $^{40}\text{Ar}/^{39}\text{Ar}$  dating of core recovered by the Hawaii Scientific Drilling Project (phase 2), Hilo, Hawaii, *Geochem. Geophys. Geosyst.*, *6*, Q04G17, doi:10.1029/2004GC000846.
- Stevelling, E. (2006), personal communication.
- Stevelling, E., J. B. Stoll, and M. Leven (2003), Quasi-continuous depth profiles of rock magnetization from magnetic logs in the HSDP-2 borehole, Island of Hawaii, *Geochem. Geophys. Geosyst.*, *4*(4), 8708, doi:10.1029/2002GC000330.
- Tan, S., Y. P. Ma, I. M. Thomas, and J. P. Wiksw (1996), Reconstruction of two-dimensional magnetization and susceptibility distributions from the magnetic field of soft magnetic materials, *IEEE Trans. Mag.*, *32*, 230–234.
- Tauxe, L., and J. J. Love (2003), Paleointensity in Hawaiian Scientific Drilling Project Hole (HSDP2): Results from submarine basaltic glass, *Geochem. Geophys. Geosyst.*, *4*(2), 8702, doi:10.1029/2001GC000276.
- Thomas, I. M., T. C. Moyer, and J. P. Wiksw (1992), High resolution magnetic susceptibility imaging of geological thin sections: Pilot study of a pyroclastic sample from the Bishop Tuff, *Geophys. Res. Lett.*, *19*, 2139–2142.
- Vacquier, V. (1962), A machine method for computing the magnitude and direction of magnetization of a uniformly magnetized body from its shape and a magnetic survey, in *Proceedings of the Benedum Earth Magnetism Symposium*, edited, pp. 123–137, Univ. of Pittsburgh Press, Pittsburgh.
- von Frese, R. R. B., W. J. Hinze, and L. W. Braile (1981), Spherical Earth gravity and magnetic anomaly analysis by equivalent point source inversion, *Earth Planet. Sci. Lett.*, *53*, 69–83.
- Walton, A. W., and P. Schiffman (2003), Alteration of hyaloclastites in the HSDP 2 Phase 1 Drill Core - 1. Description and paragenesis, *Geochem. Geophys. Geosyst.*, *4*(5), 8709, doi:10.1029/2002GC000368.
- Weiss, B. P., J. L. Kirschvink, F. J. Baudenbacher, H. Vali, N. T. Peters, F. A. MacDonald, and J. P. Wiksw (2000), A low temperature transfer of ALH84001 from Mars to Earth, *Science*, *290*, 791–795.
- Weiss, B. P., F. J. Baudenbacher, J. P. Wiksw, and J. L. Kirschvink (2001), Magnetic microscopy promises a leap in sensitivity and resolution, *Eos Trans. AGU*, *82*, 513–518.
- Weiss, B. P., H. Vali, F. J. Baudenbacher, J. L. Kirschvink, S. T. Stewart, and D. L. Shuster (2002), Records of an ancient Martian magnetic field in ALH84001, *Earth Planet. Sci. Lett.*, *201*, 449–463.
- Weiss, B. P., L. E. Fong, E. A. Lima, F. J. Baudenbacher, and H. Vali (2005), Paleointensity of the Martian field from SQUID microscopy, *Eos Trans. AGU*, *86*, Fall Meeting Suppl., Abstract GP41C-04.
- Wellstood, F. C., Y. Gim, A. Amar, R. C. Black, and A. Mathai (1997), Magnetic microscopy using SQUIDS, *IEEE Trans. Appl. Supercond.*, *7*, 3134–3138.
- Wiksw, J. P. (1996), The magnetic inverse problem for NDE, in *SQUID Sensors: Fundamentals and Frontiers*, edited by H. Weinstock, pp. 629–695, Kluwer Academic Publishers, Dordrecht.
- Wiksw, J. P. (2004), SQUIDS remain best tools for measuring brain's magnetic field, *Physics Today*, *57*, 15–17.

F. J. Baudenbacher, Department of Biomedical Engineering, Vanderbilt University, Nashville, TN 37235, USA.

L. E. Fong, Department of Physics and Astronomy, Vanderbilt University, Nashville, TN 37235, USA.

E. A. Lima and B. P. Weiss, Department of Earth, Atmospheric, and Planetary Sciences, Massachusetts Institute of Technology, Cambridge, MA 02139, USA. (bpweiss@mit.edu)